

Genetic Magnetohelioseismology with Hankel analysis data

A. D. Crouch,^{1,2*} P. S. Cally,^{2*} P. Charbonneau,^{1*}
D. C. Braun,^{3*} and M. Desjardins^{1*}

¹*Département de Physique, Université de Montréal, QC, H3C 3J7, Canada*

²*Centre for Stellar and Planetary Astrophysics, School of Mathematical Sciences, Monash University, Victoria, 3800, Australia*

³*NorthWest Research Associates, Inc., Colorado Research Associates Division, 3380 Mitchell Lane, Boulder CO 80301-5410 USA*

4 August 2005

ABSTRACT

Hankel analysis determined that sunspots absorb energy from and shift the phase of f - and p -modes incident upon them. One promising mechanism that can explain the absorption is partial conversion to slow magnetoacoustic-gravity waves and Alfvén waves, which guide energy along the magnetic field away from the acoustic cavity. Our recent mode conversion calculations demonstrated that simple sunspot models, which roughly account for the radial variation of the magnetic field strength and inclination, can produce ample absorption to explain the observations, along with phase shifts that agree remarkably well with the Hankel analysis data. In this paper, we follow the same approach, but adopt a more realistic model for the solar convection zone that includes the thermal perturbation associated with a sunspot’s magnetic field. Consistent with our earlier findings, we show that a moderately inclined, uniform magnetic field exhibits significantly enhanced absorption (mode conversion) in comparison to a vertical field (depending on the frequency and radial order of the mode). A genetic algorithm is employed to adjust the parameters that control the radial structure of our sunspot models, in order to minimize the discrepancy between the theoretical predictions and the Hankel analysis measurements. For models that best fit the phase shifts, the agreement with the Hankel analysis data is excellent, and the corresponding absorption coefficients are generally in excess of the observed levels. On the other hand, for models that best fit the phase shift and absorption data simultaneously the overall agreement is very good but the phase shifts agree less well. This is most likely caused by the different size of the regions responsible for the absorption and phase shift. Typically, the field strengths required by such models lie in the range 1 – 3 kG, compatible with observations for sunspots and active regions. While there remain some uncertainties, our results provide further evidence that mode conversion is the predominant mechanism responsible for the observed absorption in sunspots; and that field inclination away from vertical is a necessary ingredient for any model that aims to simultaneously explain the phase shift and absorption data.

Key words: Sun: helioseismology — Sun: magnetic fields — sunspots.

1 INTRODUCTION

One of the goals of local helioseismology is to determine information about the internal and subsurface structure of sunspots, by observing how solar acoustic oscillations interact with them. Hankel analysis (e.g., Braun, Duvall & LaBonte 1987, 1988; Braun et al. 1992; Bogdan et al. 1993;

Braun 1995) is one of several available techniques. It studies the interaction by decomposing the oscillation signal Ψ in an annular region surrounding (but excluding) the sunspot into components of the form

$$\Psi(\vartheta, \varphi, t) = [aH_m^{(1)}(L\vartheta) + bH_m^{(2)}(L\vartheta)] \exp[i(m\varphi + \omega t)], \quad (1)$$

where ϑ and φ are the familiar spherical polar coordinates (the spot is situated at $\vartheta = 0$), m is the azimuthal order, $L = \sqrt{l(l+1)}$ (l is the spherical harmonic degree), t is time, ω is the angular frequency, $H_m^{(1,2)}$ are the Hankel functions of the first and second kind, and a and b represent the complex amplitudes of the ingoing and outgoing waves (p -modes),

* E-mail: ash@astro.umontreal.ca (ADC);
paul.cally@sci.monash.edu.au (PSC);
paulchar@astro.umontreal.ca (PC);
dbraun@cora.nwra.com(DCB); michele@astro.umontreal.ca (MD)

respectively. Any difference between the complex amplitudes quantifies the interaction. For example, if the wave loses (gains) power during the encounter then $|b|$ will be less than (greater than) $|a|$ and the absorption coefficient,

$$\alpha = 1 - \frac{|b|^2}{|a|^2},$$

will be positive (negative). If the phase speed of the wave is increased (decreased) inside the spot then the phase (i.e., the argument) of the outgoing wave will be ahead of (behind) its incoming counterpart and the phase shift,

$$\delta = \arg(b) - \arg(a),$$

will be positive (negative).

Braun (1995) examined two very different sunspot groups using long data sets (duration $\gtrsim 64$ hours) collected at the South Pole in 1988 (Braun’s results remain the highest quality Hankel analysis data available). The sunspot in group NOAA5254 had a fairly regular appearance (nearly circular, very symmetric penumbra), with umbral radius of 9 Mm and penumbral radius of 18 Mm. The sunspot in group NOAA5229 was very irregular and slightly smaller, with umbral radius of 6 Mm and penumbral radius of 15 Mm. The annulus used for the Hankel analysis had an outer radius of 243 Mm and an inner radius of 30 Mm (chosen to exclude a central region somewhat larger than the penumbral radius of the spot in NOAA5254).

Figs. 1 and 2 show the absorption coefficients and phase shifts for the two sunspot groups that were found by Braun (1995). They illustrate several points. (1) In general, sunspots absorb and advance the phase of f - and p -modes incident upon them. (2) The absorption coefficient α increases from roughly zero at the lowest frequencies to a peak at intermediate frequencies (which can be greater than half in favourable cases), it dips to around zero and seems to rise again at the highest observed frequencies. (3) Peak absorption decreases with increasing radial order. (4) The frequency of the peak (and dip) in α is smallest for lower radial order modes. (5) The phase shift δ is generally positive, indicating that the waves are sped up inside the spot. (6) The phase shift grows rapidly from zero at lower frequencies, and the frequency at which δ starts to grow increases with radial order. (7) Despite the difference in appearance, both sunspots exhibit very similar behaviour (although the larger sunspot NOAA5254 shows consistently higher mean absorption). The final point indicates that Hankel analysis unfortunately lacks the spatial resolution to discriminate between spots of different surface morphology. For this reason we focus on NOAA5254 (the more typical) for the remainder of this investigation.

More recently, other techniques have been used to probe sunspots and their environment. Acoustic holography confirmed the findings of Hankel analysis (Lindsey & Braun 1999) and has discovered an array of seismic features such as regions of enhanced high frequency acoustic emission surrounding active regions ‘acoustic glories’ (Braun & Lindsey 1999; Donea, Lindsey & Braun 2000, see also Jain & Haber 2002), and the distortion effects associated with the ‘acoustic showerglass’ in the shallow subphotospheric layers of active regions (Lindsey & Braun 2004, 2005a,b). We will return to this point later, but it is worth noting here that quiet Sun emission phenomena like acoustic glories can reside inside

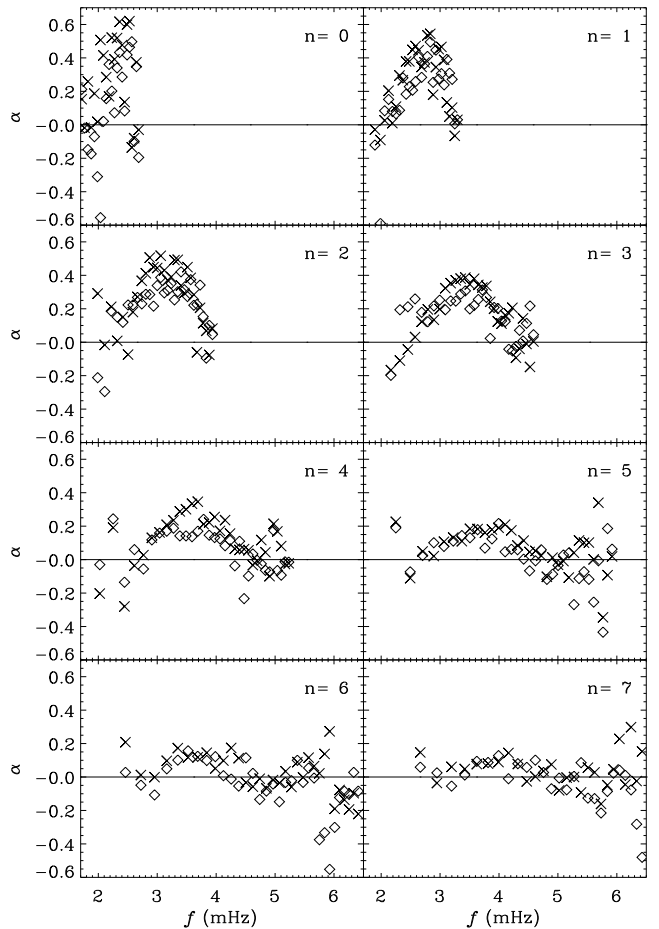


Figure 1. The m -averaged absorption coefficient α as a function of frequency f for the f -mode and p_n -modes (with radial order $n \leq 7$) for the sunspot groups: NOAA5254 (*crosses*) and NOAA5229 (*diamonds*). For clarity, error bars are not shown here, but only points with $\sigma_\alpha < 0.5$ are plotted. Adapted from the results of Braun (1995).

the annulus used by Hankel analysis. Accordingly, Lindsey & Braun (1999) suggested that the high frequency dips in α (Fig. 1) may be the result of enhanced quiet Sun emission rather than a true dip in the sunspot’s absorption.

Time-distance helioseismology (or helioseismic tomography) has revealed that mean travel times for waves propagating into or away from the umbra of sunspots are reduced by approximately half a minute (in comparison to waves propagating through quiet Sun). Duvall et al. (1996) suggested these are indicative of an increased wave speed along the acoustic ray paths. Braun (1997) compared ‘centre-annulus’ time-distance correlation travel times with phase shifts from Hankel analysis, and found that the former are systematically larger. However, this may be at least partly due to the differences between the types of measurements, in that time-distance centre-annuli correlations centred on sunspots select waves which propagate predominantly up or down through the near-surface layers of the spot where wave-speed perturbations may be substantial, while the phase shifts determined by Hankel analysis include the contribution of the waves which pass through and possibly below the sunspot at a greater depth. The agreement between

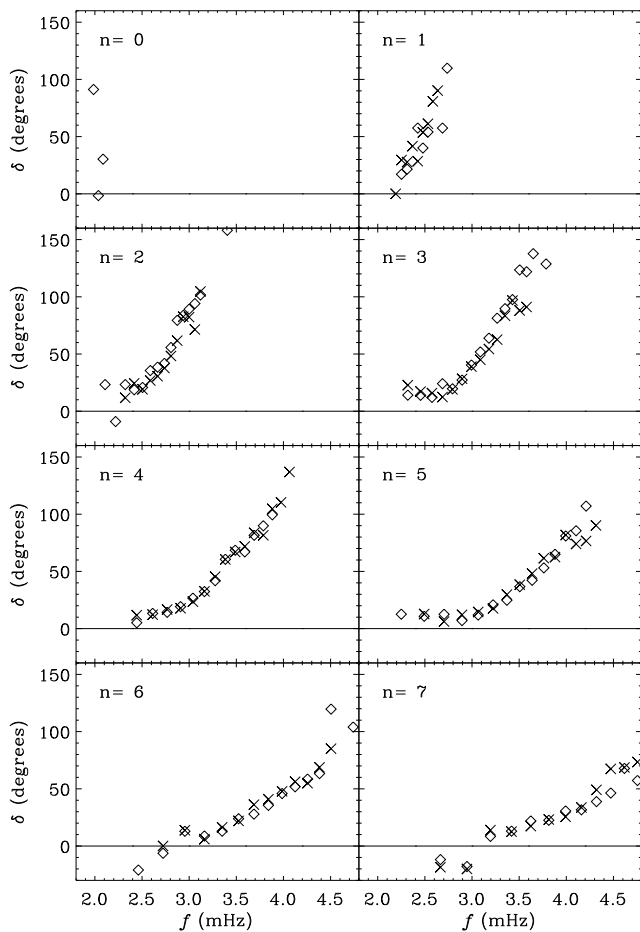


Figure 2. The m -averaged phase shift δ as a function of frequency f for the f -mode and p_n -modes (with radial order $n \leq 7$) for the sunspot groups: NOAA5254 (*crosses*) and NOAA5229 (*diamonds*). Error bars are not shown here, but only points with $\sigma_\delta < 30^\circ$ are plotted (no f -mode points satisfy this condition for NOAA5254). Adapted from Braun (1995).

the different measurements appears to improve with increasing degree l or equivalently, decreasing centre-annulus distance. Inversions of time-distance measurements have subsequently imaged the three-dimensional structure of the wave speed perturbation below sunspots (e.g., Kosovichev, Duvall & Scherrer 2000), and show a wave speed decrease in the near-surface layers below a sunspot and an increase over a broad region in the deeper layers (to depths around 10 Mm).

Hankel analysis (because it is only concerned with waves in the regions outside the spot) makes no implicit assumptions about the magnetic field. On the other hand, neither time-distance helioseismology nor holography yet incorporate magnetic fields in an entirely consistent manner (though Kosovichev & Duvall 1997 have attempted to include the fast magnetoacoustic speed in their dispersion relation). Recent theoretical and observational work on this front indicates that magnetic fields do in fact have a significant influence on the acoustics of active regions. For example, Cally (2005b) has shown that simple magnetic fields cause acoustic ray paths (the formalism often used to interpret time-distance observations) to successively split into fast and slow magnetoacoustic-gravity (MAG) wave components (the dis-

persion relation of Kosovichev & Duvall 1997 and the evaluation of mode damping effects by Kosovichev et al. 2000 neglect this complication). In addition, a horizontal magnetic field in the atmosphere overlying the convection zone can modify the p -modes in two ways: by shifting their frequencies (e.g., Campbell & Roberts 1989; Evans & Roberts 1990, 1992; Jain & Roberts 1994a,b,c, 1996) and by damping energy from them through coupling to the Alfvén and cusp resonances (e.g., Zhukov 1997; Tirry et al. 1998; Pintér & Goossens 1999; Vanlommel & Goossens 1999; Vanlommel et al. 2002). From the observational perspective, Lindsey & Braun (2005a,b) have developed magnetic proxies based on the surface field strength to correct for the showerglass effect in active regions, and have found evidence that inclined magnetic fields in active region penumbrae substantially modify helioseismic signals (see also Schunker et al. 2005).

There have been several theoretical attempts to explain the observations, but these have tended to focus on the causes of the phase shifts and absorption separately (for a detailed review see Crouch & Cally 2003). In Cally, Crouch & Braun (2003), we presented a model that accounts for the magnetic field in a simple yet physically consistent fashion which can simultaneously account for both α and δ . The mechanism that is responsible for the absorption in that model is mode conversion (as first suggested by Spruit 1991; Spruit & Bogdan 1992).

In gravitationally stratified, magnetised atmospheres (typical of sunspot interiors), mode conversion occurs because the sound speed greatly exceeds the Alfvén speed at large depth, whereas, above the surface (photosphere) the opposite is true – the Alfvén speed greatly exceeds the sound speed. At large depth, the fast and slow MAG waves and Alfvén waves are locally decoupled. The fast MAG waves are essentially acoustic trapped oscillations (much like the non-magnetic p -modes), and the slow MAG waves and the Alfvén waves are both incompressive travelling waves, which carry energy downward along the magnetic field. On the other hand, in the region where the sound speed and Alfvén speed are comparable (near the surface) the fast and slow MAG waves and the Alfvén waves are coupled – they lose their individual character and exchange energy (as shown in the WKB and perturbation analyses by Cally 2003, 2005a). When incident p -modes excite these waves in sunspot interiors they lose energy due to the partial conversion to waves that guide energy along the magnetic field.

The first models of the mode conversion process assumed a vertical magnetic field (e.g., Cally & Bogdan 1993; Cally, Bogdan & Zweibel 1994; Cally 1995; Bogdan & Cally 1997; Cally & Bogdan 1997; Rosenthal & Julien 2000). Vertical field models could adequately explain the absorption of lower order modes (such as f - and p_1 -modes), but could not fully account for the observations of the higher order p -modes. More recently, it was shown by Crouch & Cally (2003, 2005) that the absorption rates for higher order modes are substantially enhanced when the field is non-vertical (with mode conversion being most efficient at inclinations around 30° , depending on the frequency and radial order, see also Cally 2000). Subsequently, Cally et al. (2003) constructed simple sunspot models using the results of Crouch & Cally (2003). They showed that the p -mode absorption produced by models that include non-vertical field is indeed ample to account for the observations of Hankel

analysis. In addition, Cally et al. also showed that the phase shifts produced by their simple models are in excellent agreement with the observations.

In essence, this investigation is a direct extension of the work by Cally et al. (and Crouch & Cally 2003, 2005). Initially, we neglect the horizontal (radial) variation of structure observed in sunspots and concentrate on accurately accounting for the vertical variation. This assumption is reasonable in the context of sunspots where the scale of the vertical variations (the local density scale height) is typically a few hundred kilometres near the surface, whereas the scale for the horizontal variation in the surface magnetic field is of order several megametres. Previously, we modelled the solar convection zone with a complete adiabatic polytrope (Crouch & Cally 2003, 2005; Cally et al. 2003). Here, we use a more realistic representation, based on the solar model fgong.l5bi.d.15 from the Aarhus adiabatic pulsation package (Christensen-Dalsgaard 1997), see Section 2 for details.

In Section 3, we calculate horizontal wavenumber eigenvalues associated with the oscillations supported by this realistic model. These provide valuable information about how the magnetic field modifies the horizontal phase speed of the waves (i.e., induces phase shifts or travel time perturbations), along with details of the horizontal spatial decay rate (absorption) experienced by the waves.

In Section 4, we re-introduce horizontal variation back into the problem, in a very simple manner, by applying the eigenvalues to a model that consists of a set of concentric cylinders (shells). To roughly account for the observed radial variation in structure, the magnetic field strength and inclination are allowed to vary between shells. In Section 5, we then use a genetic algorithm to adjust those properties in order to minimize the discrepancy between the model predictions and the Hankel analysis data of Braun (1995). Our model is too simple to perform detailed forward modelling at this stage. Instead, we use the genetic algorithm to make extensive comparisons and critically evaluate the model and the mode conversion hypothesis.

2 STATIC EQUILIBRIUM MODEL

Unfortunately, there is no available thermal model for a sunspot that extends over the range of depths of helioseismic interest (the umbral core models of Maltby et al. 1986, are arguably the best available but cover only altitudes above $z \approx -120$ km, whereas the depth of the lower turning points for the p -modes can be at least 10 Mm below the surface). Our static equilibrium model for the solar interior is based on the realistic solar model fgong.l5bi.d.15 (hereafter GONG model) from the Aarhus adiabatic pulsation package (Christensen-Dalsgaard 1997). The GONG model is modified slightly to include the expected effect of the thermal perturbation caused by a sunspot's magnetic field. We account for the variation of pressure, density, adiabatic exponent, and gravitational acceleration (curvature of the solar surface is neglected in our calculations). Two versions of the model are considered: a non-magnetic *exterior* (i.e., the quiet Sun) and a family of magnetic *interiors* with field strengths $B = 0.5, 1.0, 1.5, 2.0, \dots, 7.5$ kG (intended to span the conditions inside a typical sunspot). Each magne-

tised model is permeated by an inclined, straight, uniform magnetic field,

$$\mathbf{B} = B (\sin \theta \hat{\mathbf{e}}_x + \cos \theta \hat{\mathbf{e}}_z),$$

where θ is the angle between the magnetic field vector and the vertical, $\hat{\mathbf{e}}_z$.

Figs. 3 – 5 show the variation of the Alfvén speed, the adiabatic exponent, and the sound speed, respectively, as a function of depth for models with different field strengths. The density profile is the same for all models, therefore, the Alfvén speed varies in a entirely predictable manner between the different cases (Fig. 3). On the other hand, for depths below the level where the temperature $T = T_t = 4500 - 1000B/3$ (T is measured in Kelvin and B in kilogauss) in the magnetised models, the gas pressure is reduced to ensure the total (gas + magnetic) pressure is constant across all models irrespective of the field strength, i.e.,

$$p_{\text{ex}} = p_{\text{in}} + \frac{B^2}{2\mu},$$

where the subscripts ‘ex’ and ‘in’ refer to exterior and interior properties, respectively. The modified gas pressure p_{in} is used to correct the adiabatic exponent Γ_1 with a simple Saha equation solver that includes the ionisation of hydrogen and helium. The effect of the magnetic pressure is strongest near the surface. This is clearly evident in Fig. 4, which shows that the nature of the large dip in Γ_1 is substantially altered by the magnetic pressure in the surface layers. At great depth, the adiabatic exponent (and the sound speed, Fig. 5) is virtually identical in each model, as the gas pressure overwhelms the magnetic pressure in that region.

At this stage, we do not intend to model the chromosphere and corona with any degree of sophistication. For simplicity, we append an isothermal slab (with $T = T_t$) to the top of the modified GONG models that extends from the upper boundary $z = z_t = 495.9$ km to the depth where $T = T_t$ (the isothermal slab is cooler and extends deeper for stronger field, in a similar fashion to a Wilson depression). Again, Fig. 5 shows that the sound speed, and hence the temperature, is most strongly affected by the magnetic field in the surface layers (elsewhere the sound speed profile is virtually indistinguishable between models). Clearly, some of the finer structural features around the temperature minimum region are missing from this model (Fig. 5), but the isothermal slab is only supposed to give the waves some distance to reflect (because we have not included the solar atmosphere, we only consider oscillations with frequencies below the acoustic cutoff in the isothermal slab, see Section 3 for discussion).

At a depth of $z = z_b = -16$ Mm we terminate the modified GONG models and append an adiabatic polytrope. This is done because analytic or semi-analytic solutions for the wave equations can be developed for the polytrope (these are discussed in detail in Section 3). In the polytrope, the adiabatic exponent is constant (we take the value for a monatomic ideal gas $\Gamma_1 = \gamma = 5/3$), the density and pressure take the usual form,

$$\rho(z) = \rho_0 \left(\frac{z_0 - z}{L} \right)^{3/2} \quad \text{and} \quad p(z) = \frac{2}{5} \rho_0 g_b L \left(\frac{z_0 - z}{L} \right)^{5/2},$$

$$z \leq z_b, \quad (2)$$

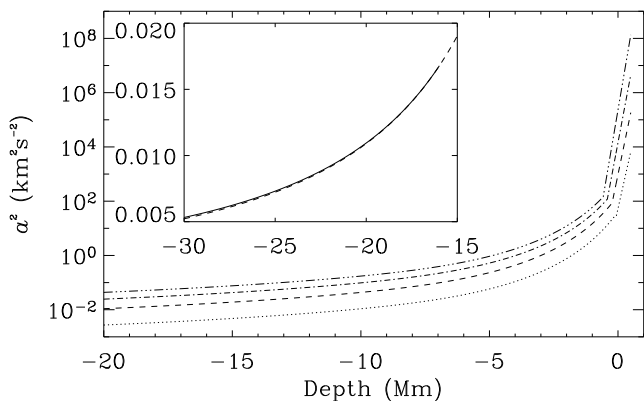


Figure 3. Squared Alfvén speed, $a^2 = B^2/\mu\rho$, as a function of depth for four of the magnetised models. The lowest *dotted curve* is the squared Alfvén speed for $B = 1$ kG, the *dashed curve* is $B = 2$ kG, the *dash-dotted curve* is $B = 3$ kG, and the *dash-dot-dotted curve* is $B = 4$ kG. The *inset* provides a comparison between the modified GONG model with $B = 2$ kG (*dashed curve*) and the corresponding polytrope (*full curve*) at great depth (they match exactly at $z_b = -16$ Mm).

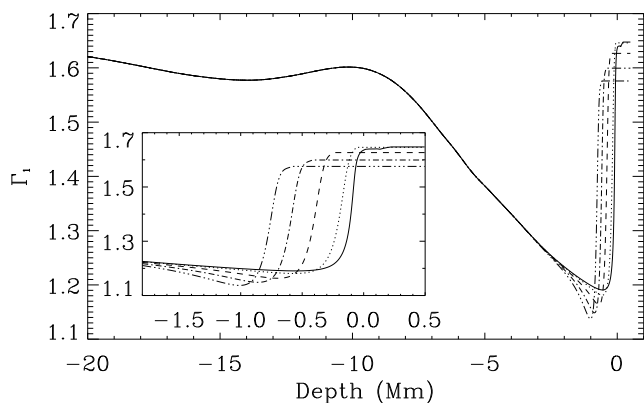


Figure 4. Adiabatic exponent, Γ_1 , as a function of depth for the non-magnetic model and four of the magnetised models. The *full curve* is Γ_1 for the non-magnetic model. For the magnetised models the curve labelling is identical to Fig. 3. The *inset* shows an expanded view of the surface layers.

and the gravitational acceleration is uniform ($g_b = g(z_b) \approx 287\text{ms}^{-2}$ is the value at the base of the modified GONG models). In the magnetic cases L is the depth below z_0 where the sound speed and Alfvén speed would coincide if equation (2) was applied all the way to the natural surface of the polytrope z_0 (where the pressure and density simultaneously vanish). In the non-magnetic case, L is arbitrary and physically meaningless (for convenience we take it as the depth where the sound speed is specified). The parameters z_0 and L are adjusted to ensure that sound speed and Alfvén speed are continuous at $z = z_b$ (numerical testing demonstrates that smoothing the transition at $z = z_b$ has little overall impact on our results). The polytrope does a very reasonable job of approximating the deeper regions of the solar interior where the adiabatic exponent is roughly constant ($\Gamma_1 \approx 5/3$, Fig. 4) and the squared sound speed is effectively linear (Fig. 5, the squared Alfvén speed also matches very well, see Fig. 3). For $z_b \lesssim -12$ Mm, numeri-

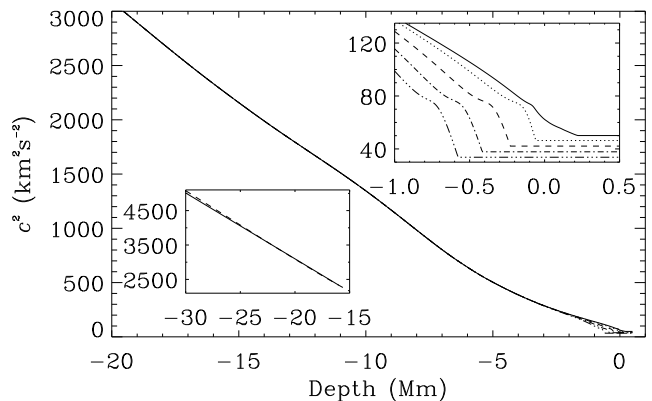


Figure 5. Squared sound speed, $c^2 = \Gamma_1 p/\rho$, as a function of depth for the non-magnetic model and four of the magnetised models. The curve labelling is identical to Fig. 4. The *inset on the lower left* provides a comparison between the modified GONG model with $B = 2$ kG (*dashed curve*) and the corresponding polytrope (*full curve*) at great depth (they match exactly at $z_b = -16$ Mm). The *inset on the upper right* shows an expanded view of the surface layers.

cal experiments indicate that our results (in particular, the eigenvalues in Section 3) are fairly insensitive to the actual value of z_b . The choice $z_b = -16$ Mm includes as much of the modified GONG models as possible, without compromising numerical accuracy and calculation time.

3 HORIZONTAL WAVENUMBER EIGENVALUES

In this section, we consider the steady state, linear, adiabatic oscillations of each model individually. The models are infinite in horizontal extent and all of their static equilibrium properties depend only on the vertical spatial coordinate, z . Therefore, it is appropriate to assume that all perturbed quantities depend on the horizontal spatial coordinates, x and y , and time according to $\exp[i(\mathbf{k}\cdot\mathbf{r} - \omega t)]$, where $\mathbf{k} = k(\cos\phi\hat{\mathbf{e}}_x + \sin\phi\hat{\mathbf{e}}_y)$ is the horizontal wave-vector and $\mathbf{r} = x\hat{\mathbf{e}}_x + y\hat{\mathbf{e}}_y + z\hat{\mathbf{e}}_z$ is the position vector. We investigate the spatial evolution of the free oscillations supported by each model by specifying the real, non-negative angular frequency ω and calculating horizontal wavenumber eigenvalues k . In addition, we assume that travelling waves propagate in the direction parallel to the unit vector $\hat{\mathbf{k}} = \cos\phi\hat{\mathbf{e}}_x + \sin\phi\hat{\mathbf{e}}_y$ (i.e., $\text{Re}(k) \geq 0$). For the non-magnetic case, the oscillations propagate without energy loss and, thus, k is purely real. On the other hand, due to mode conversion in the magnetic cases k is generally complex – the imaginary part quantifies the horizontal spatial decay rate of the oscillations.

3.1 Non-magnetic eigenvalues

In the non-magnetic exterior, the Lagrangian fluid displacement, $\boldsymbol{\xi} = \xi_x\hat{\mathbf{e}}_x + \xi_y\hat{\mathbf{e}}_y + \xi_z\hat{\mathbf{e}}_z = \zeta\hat{\mathbf{k}} + \eta\hat{\mathbf{k}}_\perp + \xi_z\hat{\mathbf{e}}_z$, (where $\hat{\mathbf{k}}_\perp = -\sin\phi\hat{\mathbf{e}}_x + \cos\phi\hat{\mathbf{e}}_y$) satisfies a second-order system of ordinary differential equations:

$$(\omega^2 - k^2 c^2)\zeta + ik(c^2 \xi'_z - g\xi_z) = 0, \quad (3)$$

$$c^2 \xi_z'' + \left(c^2 \frac{\Gamma_1'}{\Gamma_1} - \Gamma_1 g \right) \xi_z' + (\omega^2 - g') \xi_z + ik \left\{ c^2 \zeta' - \left[(\Gamma_1 - 1) g - c^2 \frac{\Gamma_1'}{\Gamma_1} \right] \zeta \right\} = 0, \quad (4)$$

where $' = d/dz$. In the non-magnetic case, no restoring forces act in the \mathbf{k}_\perp -direction, hence, $\eta = 0$.

In unmagnetised regions of the real Sun, acoustic waves propagate upward into the atmosphere only if their frequency is above the local acoustic cutoff frequency at the temperature minimum; otherwise, they are reflected by rapidly decreasing density scale height. We do not intend to model the solar atmosphere in this investigation so we must only consider frequencies below the acoustic cutoff (though it should be noted that inclined magnetic fields introduce some complications to this argument, see Section 3.2). In general, most acoustic waves (with frequencies below the cutoff) will naturally be reflected before they reach the very top of the model. The rigid lid boundary condition that we employ at $z = z_t$ is designed to reflect any residual waves that may still be propagating upward at the top boundary. Hence, we require that the vertical component of the displacement vanishes, i.e.,

$$\xi_z = 0, \quad \text{at } z = z_t. \quad (5)$$

In the adiabatic (convectively neutral) polytrope at the base, analytic solutions for the non-magnetic wave equations (equivalent versions of equations (3) and (4) with constant Γ_1 and g) can be found in terms of Confluent Hypergeometric functions (e.g., Lamb 1945; Spiegel & Unno 1962; Christensen-Dalsgaard 1980; Campbell & Roberts 1989). The physical solution, for which the associated perturbations remain bounded as $z \rightarrow -\infty$, has horizontal displacement

$$\zeta = C \exp [k(z - z_0)] U \left[a, \frac{3}{2}, 2k(z_0 - z) \right], \quad \text{for } z \leq z_b, \quad (6)$$

where $a = \frac{3}{4}(1 - \frac{\omega^2}{gk})$, U is Kummer's function (Abramowitz & Stegun 1964, equation (13.1.3)), and C is the mode amplitude. The vertical component of the displacement can be easily derived from equation (6) since $\xi_z = -i\zeta'/k$ in the polytrope.

The two point boundary value problem is then solved numerically using a bidirectional shooting method. For specified frequency ω and an initial guess for the wavenumber k , the solution that satisfies the lower boundary condition (equation (6)) is integrated upward from z_b , through the realistic solar model, to some matching point z_m . Likewise, the solution that satisfies the upper boundary condition (equation (5)) is integrated downward from z_t to z_m . In general, k must be iteratively adjusted and the solutions re-integrated until the displacement is satisfactorily continuous and smooth at the matching point. The resultant linear combination of the two solutions is the eigenfunction and the corresponding value of the wavenumber, k , is the eigenvalue.

Because we have made several simplifications (the curvature of the solar surface is neglected, a polytrope is appended to the base of our model, and the upper boundary condition is slightly artificial), we expect that the oscillations supported by our model will not perfectly match the observed oscillations. Fig. 6 shows this is indeed the case,

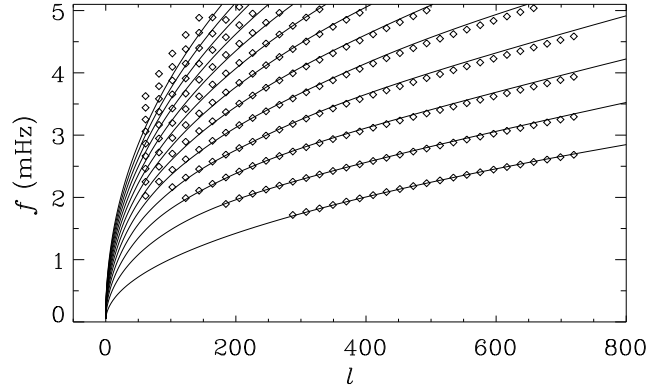


Figure 6. Frequency, f , as a function of degree, l , for our quiet Sun model (full curves). The f -mode ($n = 0$) is the lowest frequency curve. The first 12 p -modes are also shown (of progressively higher frequency). The diamonds are the observed frequencies from the data set of Braun (1995).

where we have plotted the temporal frequency as a function of the more familiar spherical harmonic degree l (using the relation $k = \sqrt{l(l+1)}/R_\odot$) for both the model and the observations. The model agrees very well with the observations for the lower order modes with moderate l . But for modes of higher radial order with smaller l (which penetrate deeper) there is a slight discrepancy (probably due to the lack of curvature in the model or the artificial base). There is also some disagreement at the very highest observed values of l (shallower modes) for the ridges $n \geq 1$ (this is most likely the result of the artificial upper boundary condition).

3.2 Magnetic eigenvalues

In the magnetic models, the Lagrangian fluid displacement satisfies a sixth-order system of ordinary differential equations:

$$a^2 [\cos^2 \theta \zeta'' - (\cos^2 \phi \cos^2 \theta + \sin^2 \phi) k^2 \zeta] + (\omega^2 - c^2 k^2) \zeta - \sin \theta a^2 [\cos \phi \cos \theta (\xi_z'' - k^2 \xi_z) - ik \sin^2 \phi \sin \theta \xi_z'] + ik (c^2 \xi_z' - g \xi_z) = -ik \sin \phi \sin \theta a^2 \partial_\parallel \eta, \quad (7)$$

$$a^2 \partial_\parallel^2 \eta + \omega^2 \eta = -\sin \phi \sin \theta a^2 \partial_\parallel \nabla \cdot \boldsymbol{\xi}, \quad (8)$$

$$\sin^2 \theta a^2 (\xi_z'' - \cos^2 \phi k^2 \xi_z) + c^2 \xi_z'' + \left(c^2 \frac{\Gamma_1'}{\Gamma_1} - \Gamma_1 g \right) \xi_z' + (\omega^2 - g') \xi_z + ik \left\{ c^2 \zeta' - \left[(\Gamma_1 - 1) g - c^2 \frac{\Gamma_1'}{\Gamma_1} \right] \zeta \right\} - \sin \theta a^2 [\cos \phi \cos \theta (\zeta'' - k^2 \zeta) - ik \sin^2 \phi \sin \theta \zeta'] = -\sin \phi \sin \theta a^2 \partial_\parallel \eta', \quad (9)$$

where $\partial_\parallel = \hat{\mathbf{B}} \cdot \nabla = ik \cos \phi \sin \theta + \cos \theta d/dz$ is the directional derivative in the direction parallel to the equilibrium magnetic field. For $\phi \neq 0$ (and $0 < \theta < 90^\circ$) the system of differential equations (7) – (9) is sixth-order and describes the propagation and interaction of the different types of MHD waves (the fast and slow MAG waves and the Alfvén

waves). When $\theta = 0$ (exactly vertical field) or $\phi = 0$ (propagation parallel to the plane containing \mathbf{B}) the Alfvén waves decouple, and the system governing the interaction of the fast and slow MAG waves is fourth order. When $\theta = 90^\circ$ (exactly horizontal field) equations (7) – (9) reduce to a second-order system – a singular limit that we do not consider here.

As in the non-magnetic case, we impose a rigid lid boundary condition at the top of the magnetic models that acts to reflect any upward propagating waves. Thus, we require that all components of the displacement vanish at the top boundary of the magnetic models,

$$\zeta = 0, \quad \eta = 0, \quad \text{and} \quad \xi_z = 0, \quad \text{at} \quad z = z_b. \quad (10)$$

As mentioned previously, this type of boundary condition is a reasonable assumption for oscillations with frequencies below the acoustic cutoff when there is no magnetic field. The same argument is not necessarily true when the atmosphere is threaded by a magnetic field. In the case of an exactly vertical magnetic field, Cally et al. (1994) found that a boundary condition similar to the rigid lid condition is valid below the acoustic cutoff frequency. The issue is more complicated when the field is non-vertical.

If we assume that the magnetised regions of the solar atmosphere above sunspots can be modelled by an isothermal layer(s) threaded by inclined uniform magnetic field then the results of Zhugzhda & Dzhililov (1984) are applicable. At great height in such an atmosphere, the Alfvén speed greatly exceeds the sound speed and the three linear MHD waves asymptotically decouple. The fast and Alfvén waves are refracted downward but the acoustic slow waves propagate upward along the magnetic field lines. Acoustic waves propagate upward when their frequency is above the acoustic cutoff because their vertical wavelength is less than the local density scale height. For the slow waves travelling up along an inclined magnetic field the scale height in the direction of wave propagation is increased by a factor of $1/\cos\theta$ and, therefore, the acoustic cutoff frequency is reduced by a factor of $\cos\theta$ (see the Frobenius analysis of Zhugzhda & Dzhililov 1984; and for the application of this effect to spicule formation see De Pontieu, Erdélyi & James 2004; De Pontieu, Erdélyi & De Moortel 2005). Consequently, the maximum frequency at which the reflective rigid lid boundary condition (equation (10)) is valid decreases as the inclination increases.

This is one of several limitations associated with our choice of upper boundary condition. Above the photosphere the assumptions that the field is straight and uniform and that the oscillations are small amplitude (i.e., linear) are unreliable (e.g., Rosenthal et al. 2002; Bogdan et al. 2003). At this stage, we do not attempt to include these effects in our present model. As a result, our model will probably underestimate the energy loss (i.e., absorption) experienced by acoustic waves traversing sunspots. The likely effect on the phase shifts of the acoustic waves is less clear.

In the polytrope at the base of the magnetic atmospheres, asymptotic solutions for the governing wave equations have been developed previously (see Crouch 2003; Crouch & Cally 2003, 2005, for details). At large depth (as $z \rightarrow -\infty$), the three different types of MHD waves locally decouple and the requirements that evanescent modes be decreasing and wave-like disturbances be outgoing select

Table 1. Equipartition depth in the various magnetic models.

Field strength (kG)	Equipartition depth (Mm)
0.5	0.187
1.0	-0.014
1.5	-0.169
2.0	-0.323
2.5	-0.462
3.0	-0.604
3.5	-0.730
4.0	-0.843
4.5	-0.944
5.0	-1.033

three distinct solutions. The fast MAG waves are vertically trapped acoustic waves. Consequently, the fast wave components of the π -modes¹ are successively refracted at great depth back toward the conversion layer, where the various MHD waves are coupled. The slow MAG wave and Alfvén wave components are downward travelling, incompressive oscillations (driven predominantly by magnetic tension). At great depth, they carry energy away from the conversion layer and, therefore, are responsible for the decaying amplitude (i.e., absorption) of the π -modes as they traverse the magnetic models.

The different types of MHD waves interact most strongly in regions where the sound speed and Alfvén speed are comparable (i.e., near the surface in our magnetic models). The equipartition depth, where $c = a$, therefore provides a good proxy for the location of the conversion layer. Table 1 shows the equipartition depth for a selection of the magnetic models and gives the reader an idea of where the coupling between the different waves is strongest in each case. It is worth noting that the recent ray-based analysis of Cally (2005b) indicates that mode coupling typically occurs near the equipartition depth, though further coupling may also take place near the acoustic cutoff depth.

3.2.1 Results

The sixth-order two point boundary value problem is solved numerically using a bidirectional shooting method in an analogous fashion to that described in Section 3.1 (see also Crouch 2003). A selection of the results is displayed in Figs. 7 – 10 where the complex wavenumber eigenvalue k is plotted as a function of frequency, inclination, and propagation direction. Crouch & Cally (2003); Crouch (2003); Crouch & Cally (2005) studied the inclined field oscillation equations for the complete adiabatic polytrope. It is noteworthy that our results confirm their conclusions hold true when a more realistic approximation of the solar interior is employed.

Mode conversion in magnetised models such as those considered here is a very rich and complicated process (for more details see the various case studies by Rosenthal et al. 2002; Bogdan et al. 2003; Cally 2005a,b). However, a general

¹ As in our previous work, we label the solutions of the magnetic oscillation equations π -modes (i.e., p -modes modified by the magnetic field).

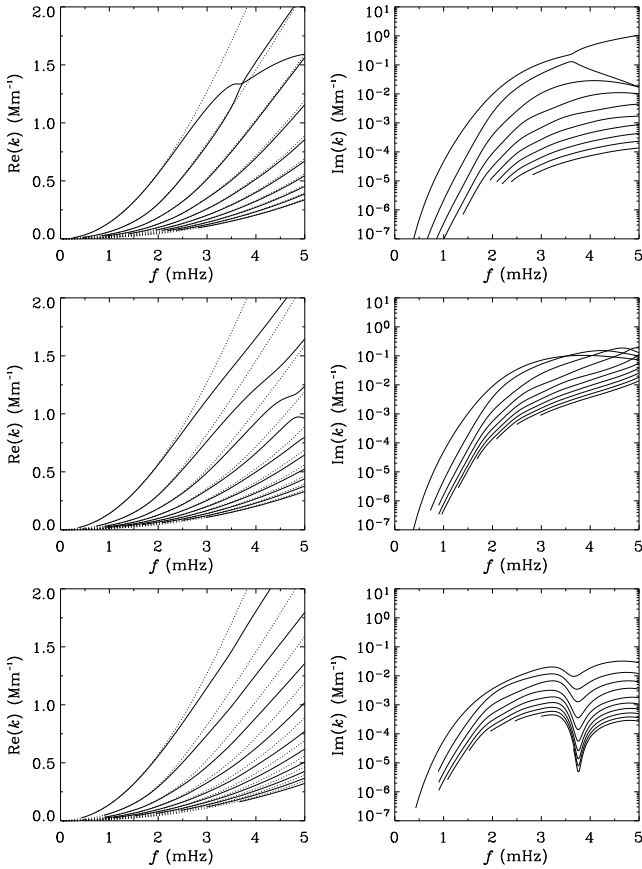


Figure 7. Wavenumber eigenvalues k as a function of frequency f for the π -modes with $n = 0, \dots, 9$. In each case, the panel on the left shows the real part of k as a function of f . The panel on the right shows the imaginary part of k as a function of f corresponding to the real part shown on the left. In general, at lower frequencies both $\text{Re}(k)$ and $\text{Im}(k)$ are largest for $n = 0$ and decrease with increasing radial order n , allowing different overtones to be distinguished easily. In the left-hand panels the eigencurves of the non-magnetic p -modes (adapted from Fig. 6) are also plotted as *light dashed lines*. For all these graphs the magnetic field strength is fixed at $B = 2$ kG and the propagation direction is fixed at $\phi = 0$ (so the Alfvén waves are decoupled in all these cases). The *top panels* show results for exactly vertical field $\theta = 0$, the *middle panels* $\theta = 30^\circ$, and the *bottom panels* $\theta = 60^\circ$.

pattern of behaviour is evident in Fig. 7. At low frequencies the π -modes are only weakly affected by the magnetic field: $\text{Re}(k)$ is essentially indistinguishable from the non-magnetic wavenumber; and the level of mode conversion (as indicated by $\text{Im}(k)$) is comparatively low. At higher frequencies the π -modes are more strongly affected by the field: in comparison to the non-magnetic p -mode ridges, the phase speed $\omega/\text{Re}(k)$ is increased in most cases; and $\text{Im}(k)$ increases by several orders of magnitude as the frequency increases from $f \approx 1$ mHz to $f \approx 3$ mHz.

Broadly speaking, this behaviour can be explained by considering the asymptotic behaviour of the π -modes at large depth. Asymptotically, the slow MAG wave (and Alfvén wave) components of the π -modes are small wavelength oscillations travelling down the magnetic field away from the conversion layer(s); whereas the acoustic fast MAG

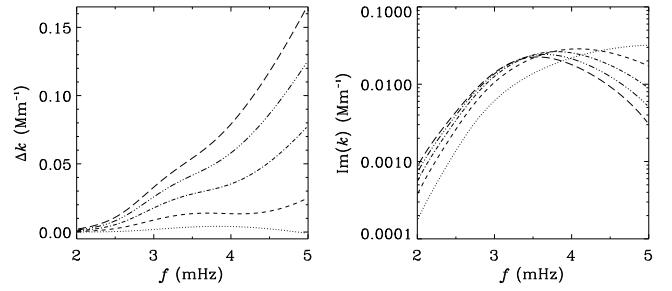


Figure 8. Wavenumber eigenvalues k as a function of frequency f for the π_2 -mode. The panel on the left shows the wavenumber shift, $\Delta k = k_0 - \text{Re}(k)$, as a function of f (where k_0 is the non-magnetic wavenumber for the p_2 -mode). The panel on the right shows the imaginary part of k as a function of f . For these graphs the magnetic field is exactly vertical ($\theta = 0$, hence, the Alfvén waves are decoupled). Each curve corresponds to a different field strength, B . The curve labelling is identical to Fig. 3: the *dotted curve* is for $B = 1$ kG, the *dashed curve* is $B = 2$ kG, the *dash-dot curve* is $B = 3$ kG, the *dash-dot-dotted curve* is $B = 4$ kG, and the *long-dashed curve* is $B = 5$ kG. The effect of the increasing field strength on this mode is clear: the magnitude of the wavenumber shift, Δk , grows with increasing B (most dramatically at higher frequencies); and $\text{Im}(k)$ increases with increasing B at lower frequencies (the change in $\text{Im}(k)$ between ridges is largest for lower field strengths and tends to saturate at higher field strengths).

wave components are successively refracted from the deeper layers back toward the surface (where the conversion layer resides, see Table 1, and the magnetic effects are strongest, see Figs. 4 and 5). For the fast waves, every successive encounter with the conversion layer will induce further mode conversion (though the exact nature of this is dependent on properties such as the frequency, wavenumber, field inclination, and stratification). The deviation of the phase speed ($\text{Re}(k)$) from the non-magnetic value also originates near the surface, though over a region broader than the conversion layer(s). At low frequencies, the fast waves have less encounters with the surface layers per unit length on average for the two following reasons: firstly, the π -modes have comparatively long horizontal wavelengths (low $\text{Re}(k)$); and, secondly, the fast waves have relatively deep exponential tails (or turning points, note: they have asymptotic controlling factor $\exp(k(z - z_0))$). On the other hand, at higher frequencies (large $\text{Re}(k)$), the fast wave components are confined closer to the surface and the horizontal wavelength of the π -modes is smaller. Consequently, at higher frequencies the fast waves have more encounters with the surface layers (per unit length) and, therefore, a greater chance of inducing mode conversion (on average). Along a given ridge, Fig. 7 indeed shows that both $\text{Im}(k)$ and the difference between the magnetic and non-magnetic wavenumbers, $\Delta k = k_0 - \text{Re}(k)$, increase with frequency (where k_0 is the non-magnetic wavenumber). These effects are also noticeable from ridge to ridge (Fig. 7): because they tend to have smaller $\text{Re}(k)$ modes of higher radial order have smaller $\text{Im}(k)$ and Δk (at fixed f).

The magnetic field affects the oscillations in two main ways. Firstly, the phase speed $\omega/\text{Re}(k)$ tends to increase (i.e., $\text{Re}(k)$ decreases and Δk increases). It is worth noting that this occurs even though the sound speed is slightly

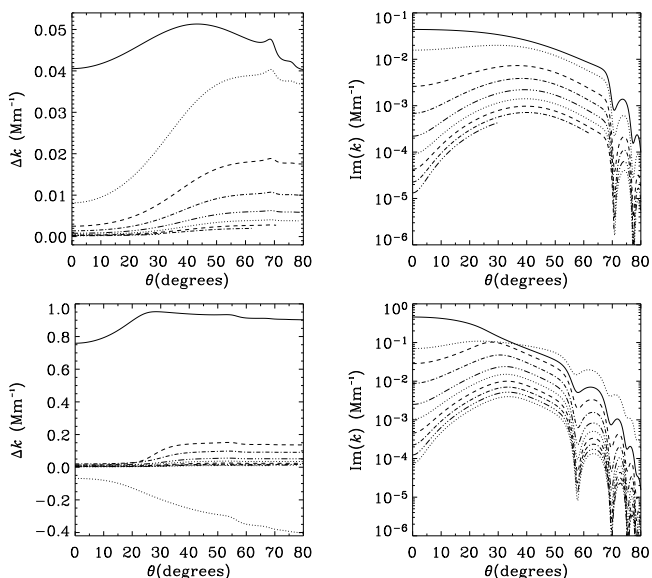


Figure 9. Wavenumber eigenvalues k as a function of inclination θ . In each case, the panel on the left shows the wavenumber shift, $\Delta k = k_0 - \text{Re}(k)$, as a function of θ (where k_0 is the non-magnetic wavenumber at the same frequency and radial order). The panel on the right shows the imaginary part of k as a function of θ . The *full curve* is π_0 , the *dotted curves* are π_1 , π_5 , and π_9 , the *dashed curves* are π_2 and π_6 , the *dash-dotted curves* are π_3 and π_7 , and the *dash-dot-dotted curves* are π_4 and π_8 . Solutions with the same curve type can be distinguished since higher order modes have smaller $\text{Im}(k)$ (when $\theta \approx 0$) and smaller magnitude Δk (for all inclinations in most cases). For all these graphs the magnetic field strength is fixed at $B = 2$ kG and the propagation direction is fixed at $\phi = 0$ (Alfvén waves are decoupled). The *top panels* show results for $f = 2.5$ mHz (for π -modes $n \leq 8$) and the *bottom panels* show $f = 4$ mHz (for π -modes $n \leq 9$).

diminished in the surface layers of our magnetic models (Fig. 5). Secondly, the amplitude of the mode decays as it propagates through the magnetic models (i.e., $\text{Im}(k) \neq 0$). As expected, Fig. 8 shows that the impact of both of these effects grows with increasing field strength in the magnetic models (note: the mode with $n = 2$ in exactly vertical field is fairly typical of the general behaviour of other modes at most inclinations).

Large dips in $\text{Im}(k)$ indicate regions of the parameter space where the fast and slow MAG waves (and Alfvén waves) are only weakly coupled. There are several examples of this phenomena in our graphs: at $f \approx 3.8$ mHz in the lower right-hand panel of Fig. 7 ($\theta = 60^\circ$); at higher frequencies in the right-hand panel of Fig. 8 (the dip occurs at lower frequencies in stronger and more inclined field); and in highly inclined field in the right-hand panels of Fig. 9. It is tempting to associate these dips with those in α at moderate frequencies in Fig. 1; indeed, in Section 5 we will show that they are important when making comparisons with the observed absorption coefficients.

Perhaps the most important feature of Fig. 7 is the dramatic rise in $\text{Im}(k)$ for the π -modes with $n \geq 1$ as the field inclination increases from vertical ($\theta = 0$, top right-hand panel) to $\theta = 30^\circ$ (middle right-hand panel). Fig. 9 shows this effect in more detail, where the wavenumber eigenvalues k are plotted as a function of inclination. For all modes

with $n \geq 1$, $\text{Im}(k)$ increases with inclination to a peak at $\theta \approx 30^\circ - 40^\circ$, which can be over an order of magnitude above the value in vertical field ($\theta = 0$). The enhancement is largest at higher frequencies (bottom panel of Fig. 9) and for modes of higher radial order. For the $n = 0$ mode $\text{Im}(k)$ is largest in vertical field (and slightly non-vertical field). As the field inclination approaches horizontal, the efficiency of mode conversion tends to diminish. Consequently, $\text{Im}(k)$ is fairly small for all modes in the bottom right-hand panel of Fig. 7 ($\theta = 60^\circ$) and in highly inclined field ($\theta \gtrsim 60^\circ$, right-hand panels of Fig. 9). Although the approximations are not strictly applicable to the modal results presented here, recent WKB and ray-based calculations by Cally (2005a,b) indicate that mode conversion indeed depends most crucially on the attack angle that the acoustic ray makes with the magnetic field lines at the equipartition depth and, therefore, moderately inclined field will generally be more conducive to mode conversion than vertical field.

The wavenumber shifts Δk are less dramatically affected by the field inclination. However, the left-hand panels of Fig. 9 show that most π -modes undergo a transition (where the inclination causes the magnitude of the shifts to increase substantially) over the range from $\theta \approx 20^\circ$ to $\theta \approx 60^\circ$ (the same range of angles where the decay rate is greatest). This effect has important consequences for the phase shifts produced by the sunspot models in Section 5.

The other angle of interest in this problem is the propagation direction ϕ . Fig. 10 summarises the typical effect that ϕ has on the eigenvalues. The real parts of the eigenvalues are basically unaffected by the variation of ϕ in all cases (Fig. 10, top panels). The same is true for the imaginary parts, except in highly inclined field (Fig. 10(b), middle panel) where a substantial local maximum in $\text{Im}(k)$ is attained at $\phi = 90^\circ$ (in the polytrope, Crouch & Cally 2005 found a local maximum in $\text{Im}(k)$ at $\phi = 45^\circ$ when $\theta = 80^\circ$). Clearly, the efficiency of mode conversion in highly inclined field is very sensitive to the exact nature of the atmosphere (i.e., the stratification) along with the parameters θ and ϕ (the presence of several decoupling troughs at large inclinations in the right-hand panels of Fig. 9 is also indicative of this). The magnitude of $\text{Im}(k)$ at the peak at $\phi = 90^\circ$ (Fig. 10(b), middle panel) tends to be lower than the peak found at more moderate inclinations ($\theta \approx 30^\circ$, Fig. 10(a), middle panel).

Our results indicate that the eigenvalues k are generally symmetric about $\phi = 90^\circ$ (i.e., $k(\omega, \theta, \phi) = \kappa(\omega, \theta, 180^\circ - \phi)$). However, the middle panel of Fig. 10(b) shows that there is a slight asymmetry between $\phi \approx 0$ and $\phi \approx 180^\circ$ for higher order modes – this is probably due to an accumulation of numerical noise when integrating through the realistic solar model. This property is consistent with the results of Crouch & Cally (2003); Crouch (2003); Crouch & Cally (2005), although we have not been able to prove the symmetry is generally the case.

In a non-vertical field when $\phi \neq 0$ ($\phi \neq 180^\circ$), π -mode damping is due to combination of both the slow MAG waves and the Alfvén waves carrying energy down along the magnetic field. The fractional contribution by the Alfvén waves to the asymptotic wave energy flux, F_a , is plotted in the bottom panels of Fig. 10 (details of how F_a is calculated are provided by Crouch & Cally 2005, note: it is defined such that the slow MAG wave contribution is given by $F_s = 1 - F_a$).

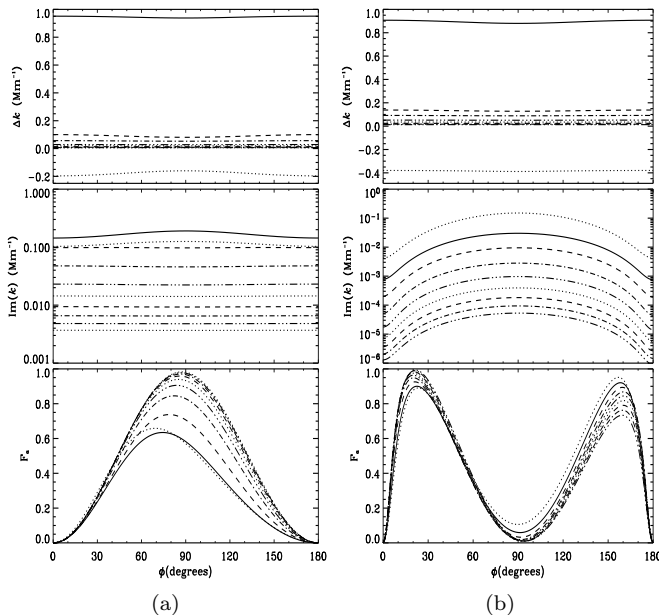


Figure 10. Wavenumber eigenvalues, k , and the contribution by the Alfvén waves to asymptotic wave energy flux, F_a , as a function of propagation direction ϕ . On both sides, the *top panel* shows the wavenumber shift, $\Delta k = k_0 - \text{Re}(k)$ (where k_0 is the non-magnetic wavenumber at the same frequency and radial order), as a function of ϕ . The *middle panel* shows the imaginary part of k as a function of ϕ , and the *bottom panel* displays the corresponding variation of F_a . The curve labelling is identical to Fig. 9. To distinguish modes with the same curve type the usual rules-of-thumb apply: higher order modes tend to have smaller $\text{Im}(k)$ and smaller magnitude Δk . For both of these graphs the magnetic field strength is fixed at $B = 2$ kG and the frequency is fixed at $f = 4$ mHz. (a) The field inclination is fixed at $\theta = 30^\circ$ (and π -modes $n \leq 9$ are displayed). (b) $\theta = 70^\circ$ (π -modes $n \leq 8$).

When $\phi = 0$ or $\phi = 180^\circ$ the Alfvén waves decouple (due to a geometric symmetry) and, therefore, $F_a = 0$ (likewise when the field is exactly vertical $\theta = 0$). Fig. 10 shows that the nature of mode conversion (as indicated by F_a) is highly dependent on the propagation direction ϕ (along with frequency, field inclination, and radial order, see Crouch & Cally 2005, for a more thorough analysis). For example, in moderately inclined fields ($\theta \approx 30^\circ$), the Alfvén waves contribute to the damping most strongly when $\phi \approx 90^\circ$ (see Fig. 10(a), lower panel); whereas in highly inclined fields ($\theta \approx 70^\circ$), they dominate when $\phi \approx 20^\circ$ and $\phi \approx 160^\circ$ (see Fig. 10(b), lower panel). However, rather than radiating great quantities of additional energy, the Alfvén waves tend to compensate in regions of the parameter space where the slow MAG waves are only weakly coupled, and visa versa. Therefore, the overall (combined) damping rate (as indicated by $\text{Im}(k)$) is fairly insensitive to changes in the propagation direction. Broadly speaking, the field inclination θ is the more significant of the two angles (as was concluded by Crouch & Cally 2005). Subsequently, for the remainder of this investigation we concentrate only on cases with $\phi = 0$ where the Alfvén waves are decoupled.

4 SIMPLE SUNSPOT MODELS

We now re-introduce horizontal/radial spatial variation by constructing very simple models for the interaction between sunspots and their surroundings (in the same fashion as Cally et al. 2003). The models consist of a set of concentric cylinders (or shells) embedded in the non-magnetic exterior. Inside each shell we decompose the various perturbed quantities into components of the form

$$\Psi(r, \varphi, z, t) = \hat{\Psi}(z) Z_m(kr) \exp[-i(m\varphi + \omega t)], \quad (11)$$

where Ψ represents any one of the perturbed quantities (e.g., horizontal displacement, pressure, etc.), Z is a Bessel function or linear combination of them (J , Y , or the Hankel functions $H^{(1,2)}$), r is the radial coordinate (taking the place of ϑ since we are working in cylindrical rather than spherical coordinates, as in equation (1)), and all other variables are the same as those defined earlier. We assume that the horizontal wavenumber eigenvalues k apply to each shell as a whole (at least on average). To capture the effects of radial structure, the magnetic field strength B and inclination θ are allowed to vary from shell to shell. Consequently, each shell has its own family of eigenvalues k (as calculated in the previous section for given B and θ). The sole purpose of the magnetic field in this model is to supply k (it plays no other role).

In the inner shell, Z_m must be the J_m Bessel function for the solution to be bounded at $r = 0$, whereas in the non-magnetic exterior, it is a linear combination

$$Z_m(k_0 r) = \mathcal{B} H_m^{(1)}(k_0 r) + H_m^{(2)}(k_0 r) \quad (12)$$

corresponding to outgoing and incoming waves, respectively (recall: k_0 is the non-magnetic wavenumber, and note: we have applied an arbitrary normalization where the amplitude of the incoming wave is set to unity). In any intervening shells, Z_m is a linear combination of J_m and Y_m . Across each shell boundary $r = R_s$ ($0 < R_1 < \dots < R_N$, where the subscript s is the label for each shell and N is the number of shells), $Z_m(kr)$ and $dZ_m(kr)/dr$ must be continuous to ensure that the total pressure and the radial velocity match (see discussion point (1) below). This allows all the coefficients in the Bessel linear combinations to be determined. Then, from \mathcal{B} , we calculate the absorption coefficient α and phase shift δ using

$$\alpha_{\text{eig}} = 1 - |\mathcal{B}|^2, \quad \delta_{\text{eig}} = -\arg(\mathcal{B}),$$

where the subscript ‘eig’ is intended to emphasize that these are model predictions based on the eigenvalues derived in Section 3 (note: excluding the depth dependence $\hat{\Psi}$, equations (11) and (12) represent the complex conjugate of equation (1) provided $\mathcal{B} = b^*$). In addition to the issues already discussed in Section 3, this model has several limitations which warrant further discussion.

(1) The acoustic jacket is ignored. Bogdan & Cally (1995) showed that the oscillations in the non-magnetic regions immediately surrounding sunspots must be decomposed in terms of both a discrete spectrum of horizontally travelling p -modes along with a continuous spectrum of horizontally evanescent jacket modes. The jacket modes are necessary because the (vertically evanescent) p -modes alone cannot perfectly match the horizontal displacement (and pressure) of the π -modes at great depth, due to the

presence of the small vertical wavelength downward travelling slow MAG waves. The matching problem, including the jacket modes, was addressed by Barnes & Cally (2000) for a thin-disk scattering model consisting of two different non-magnetic regions. The mathematical complications are severe so we do not concern ourselves with this here.

(2) Mode-mixing is neglected. In reality, an incident p -mode, with frequency f , radial order n , and azimuthal order m , will excite the complete set of outgoing p -modes of the same frequency but with different values of n and/or m . Braun (1995) found strong observational evidence for mode mixing between adjacent radial orders in both NOAA5229 and NOAA5254, but detailed measurements have not yet been made. Barnes & Cally (2000) found that mode-mixing occurs in their sunspot models but most of the energy remains in the original overtone. We neglect this effect altogether, by assuming that the non-magnetic p -mode excites only the magnetic π -mode of the same frequency and radial order (and visa versa).

This highlights an important point: mode labelling is crucial. In Crouch & Cally (2003) we pointed out that there is some ambiguity to how various overtones are labelled in inclined magnetic field (due to the complex topology of the eigenvalues over the (f, θ) -plane). We adopt the usual convention: a π -mode is labelled n if its ridge matches the ridge of the non-magnetic p_n -mode in the low frequency limit (where the magnetic field has least impact, see Fig. 7).

(3) Apart from the absorption and phase shift occurring within the spot, there are several other processes at work in and around sunspots that are not accounted for by our model (yet may impact the Hankel analysis data): the suppression of acoustic emission and finite mode lifetime effects (Bogdan et al. 1993; Braun 1995); the influence of nearby magnetic plage; and the enhancement of acoustic emission in ‘acoustic glories’ (e.g., Braun & Lindsey 1999; Donea et al. 2000; Jain & Haber 2002). As Lindsey & Braun (1999) pointed out, the high frequency dips in α (Fig. 1) may be a result of enhanced quiet Sun emission (in glories) rather than a true dip in the absorption occurring within the sunspot, which suggests the absorption inferred by Hankel analysis at higher frequencies may be an underestimate.

With these caveats in mind, we now ask ourselves: how well can these simple sunspot models (based on the eigenvalues calculated in Section 3) match Braun’s Hankel analysis data?

5 GENETIC MAGNETOHELIOSEISMOLOGY

This is a data inversion problem subject to the usual difficulties associated with non-uniqueness and noise amplification (see e.g., Craig & Brown 1986; Parker 1994). In practice, solutions can be obtained by forward modelling, whereby a ‘guess’ is made at the underlying structural model, associated (theoretical) phase shifts and absorption coefficients are computed and compared to the actual data via some goodness-of-fit measure (such as χ^2), and the original guess is improved in such as way as to reduce the discrepancy between the model predictions and observations. This turns the inverse problem into an optimization problem for the model parameters.

Because of the high dimensionality and expected multi-

modality of the search space associated with our model, we opted for a genetic algorithm-based optimizer, more specifically the subroutine PIKAIA (Charbonneau 1995), which is designed to maximise a user supplied fitness function $\mathcal{F}(\mathbf{x})$ over a bounded d -dimensional space, where $\mathbf{x} = (x_1, x_2, \dots, x_d)$ and $0 \leq x_q \leq 1$ (for each q). Such a genetic algorithm-based technique has already proved its worth in other helioseismic contexts (Charbonneau et al. 1998, 1999).

We define two variables that quantify the discrepancy between a given model and the observations:

$$\Delta\alpha^2 = \sum_{i=1}^{N_\alpha} \left(\frac{\alpha^i - \alpha_{\text{eig}}^i}{\sigma_\alpha^i} \right)^2, \text{ and } \Delta\delta^2 = \sum_{j=1}^{N_\delta} \left(\frac{\delta^j - \delta_{\text{eig}}^j}{\sigma_\delta^j} \right)^2,$$

where α^i (α_{eig}^i) and δ^j (δ_{eig}^j) represent the observed (theoretical) absorption coefficient and phase shift at data points i and j , respectively, and σ_α^i and σ_δ^j are the error estimates associated with each measurement (details of how these are calculated can be found in Braun 1995). Only observational data points with $\sigma_\alpha < 0.2$ or $\sigma_\delta < 18^\circ$ are considered in our analysis (this is fairly arbitrary, but the idea is to retain the most reliable observations). For the m -dependent data there are 1738 absorption and 1761 phase shift observations that satisfy these selection criteria; for the m -averaged data the numbers are 207 and 95, respectively (N_α and N_δ may be less than or equal to these depending on the extent of the eigenvalues for a given model). Depending on the type of data we intend to model, χ^2 (the sum of the relative discrepancies, $\Delta\alpha^2$ and/or $\Delta\delta^2$, normalised by the total number of degrees of freedom available) takes a slightly different form; for the absorption

$$\chi_\alpha^2 = \frac{\Delta\alpha^2}{N_\alpha - d},$$

for the phase shift

$$\chi_\delta^2 = \frac{\Delta\delta^2}{N_\delta - d},$$

and for the combination of both

$$\chi_t^2 = \frac{\Delta\alpha^2 + \Delta\delta^2}{N_\alpha + N_\delta - d},$$

where $d = 3N - 1$ is the number of parameters defining the model (each shell has 3 parameters: B_s , θ_s , and R_s , but $\theta_1 = 0$ by assumption, see below). The fitness of a particular model is then given by $\mathcal{F} = 1/\chi^2$.

Each input x_q for the fitness function is associated with one of the parameters B_s , θ_s , or R_s . A mapping is constructed to ensure each of these remains within the bounds of the tabulated values (or desired domain), and that the following additional restrictions are met. (1) The shells must be at least 1 Mm thick (i.e., $\min(W_s) = 1$ Mm, where W_s is the radial width of each shell such that $R_s = R_{s-1} + W_s$). The eigenvalue calculations assumed that the models were horizontally uniform. Consequently, for the eigenvalues to be valid the shells must not be too thin. The choice of 1 Mm, though arbitrary, is representative of the typical horizontal/radial scales observed in sunspots but remains significantly larger than the vertical scales (the density scale height is roughly a few hundred kilometres near the surface). (2) The magnetic field is vertical in the inner shell (i.e., $\theta_1 = 0$) and the magnetic field strength (inclination) decreases (increases) monotonically with radius (i.e.,

$B_s \geq B_{s+1}$ and $\theta_s \leq \theta_{s+1}$ for each shell s). This roughly accounts for the familiar structure of a typical sunspot, where the umbra is associated with strong nearly vertical field and the penumbra with weaker inclined field. (3) The maximum allowed radius of the sunspot is 30 Mm (i.e., $\max(R_N) = 30$ Mm), which corresponds to the inner radius of the Hankel annulus. (4) We only consider five shell models (i.e., $N = 5$). (5) Each shell has the same maximum width $\max(W_s) = \max(R_N)/N = 6$ Mm.

As was done in Cally et al. (2003), before making any comparisons we adjust the quiet Sun frequencies to correct for the slight discrepancy between the model results and the observations (Fig. 6). For a given frequency f and radial order n , the value of the corresponding spherical harmonic degree l is read from the tables of Braun (1995) and used to calculate $k_0 = \sqrt{l(l+1)}/R_\odot$. The effective frequency associated with k_0 for our quiet Sun model can then be found. Consequently, when two data points are compared, this procedure ensures that they have the same horizontal wavenumber (which makes frequency dependent comparisons more reliable). Numerical experiments demonstrate that this tends to improve the agreement between the observed and theoretical phase shifts.

We have families of magnetic eigenvalues k tabulated for field strengths $B = 0.5, 1.0, 1.5, 2.0, \dots, 7.5$ kG and inclinations $\theta = 0, 5^\circ, 10^\circ, \dots, 60^\circ$ (each family consists of radial orders $n = 0, 1, \dots, 9$ where most but not all frequencies f with acceptable observations are covered). The genetic algorithm PIKAIA searches this parameter space for the globally optimal solution (i.e., the model with smallest χ^2). For a 5-shell model with vertical field in the inner-most shell, this yields a 14-dimensional search space, with monotonicity constraints on the B_s and θ_s , and a global-sum constraint on the R_s . From the computational point of view, the constrained optimization problem so defined is also of a mixed nature, involving as it does parameters that can assume continuous (radii of shells) and discrete (inclination angle and field strength) values. All of this poses no problem for a forward modelling-based optimization scheme such as our genetic algorithm, since all model parameters, whether floating-point or integer quantities, end up being encoded along each other on the same string, on which the genetic algorithm's breeding operators then act to produce successive generations of trial solutions. Furthermore, constraints can be accommodated directly at this encoding level, thus avoiding the production of trial solutions that end up being eliminated because they do not satisfy the constraints.

For comparisons to the observational data of NOAA5254 we examine 10 evolutionary runs consisting of a population of 100 trial solutions left to evolve over 5000 generations. This requires a total of 5×10^6 model evaluations and, thus, the chance of missing the global solution is very small. However, given the limitations of the model and, to a lesser extent the observations, any attempt at quantitative forward modelling would be overly ambitious at this stage. Instead, we discuss the two best solutions from the 10 runs in the context of testing our sunspot model and the mode conversion hypothesis.

Table 2. The two models that produce best fits for the m -averaged phase shift data (i.e., minimal χ_δ^2).

MODEL A ($\chi_\alpha^2 = 34.71$, $\chi_\delta^2 = 1.077$, $\chi_t^2 = 23.91$)

Shell	1	2	3	4	5
B_s (kG)	5.5	5	3.5	3	1
θ_s (degrees)	0	0	0	0	55
R_s (Mm)	5.88	11.86	15.87	20.33	23.56

MODEL B ($\chi_\alpha^2 = 32.38$, $\chi_\delta^2 = 1.084$, $\chi_t^2 = 22.41$)

Shell	1	2	3	4	5
B_s (kG)	6	5	3.5	2.5	1
θ_s (degrees)	0	0	0	0	60
R_s (Mm)	5.78	11.78	17.06	20.91	23.04

5.1 Results

5.1.1 Modelling the m -averaged phase shift data

To improve the signal-to-noise ratio Braun (1995) averaged the absorption coefficients and phase shifts over a small range of azimuthal orders about $m = 0$ (those results were displayed in Figs. 1 and 2). Cally et al. (2003) demonstrated that the polytropic version of our sunspot model produces phase shifts that agree very well with the m -averaged observations. For this reason we initially concentrate on finding models whose axisymmetric modes ($m = 0$) best fit the m -averaged phase shift data (models for the m -dependent data will be addressed later).

The parameters describing the two models that best fit the m -averaged phase shift data are given in Table 2. Both models are very similar: the four inner-most shells contain only vertical field (whose strength decreases gradually with radius), and both have outer shells with weak, highly inclined field. The tendency of MODEL A and MODEL B to favour vertical field is compatible with the finding that models with only vertical field can also match the observed m -averaged phase shifts quite well (as found by numerical experiments, though the corresponding absorption levels produced by vertical field models for the higher modes are insufficient).

We have not imposed any restrictions on the total radii of our model sunspots R_N (except that they must be less than or equal to 30 Mm). Both MODEL A and MODEL B have similar total radii, which are somewhat larger than the observed penumbral radius of NOAA5254 (18 Mm). This is not entirely unexpected because the phase shifting region is generally considered to be a little larger than the visible size of the penumbra (e.g., Fan, Braun & Chou 1995 suggest $R \approx 25$ Mm).

Typical sunspots, like the one in NOAA5254, tend to have surface field strengths no greater than around 3.5 kG (though in reality the field will likely concentrate with depth). We have deliberately supplied PIKAIA with a range of field strengths that cover the expected range and beyond. The central field strengths in both MODEL A and MODEL B are a little higher than expected for the surface field. Per-

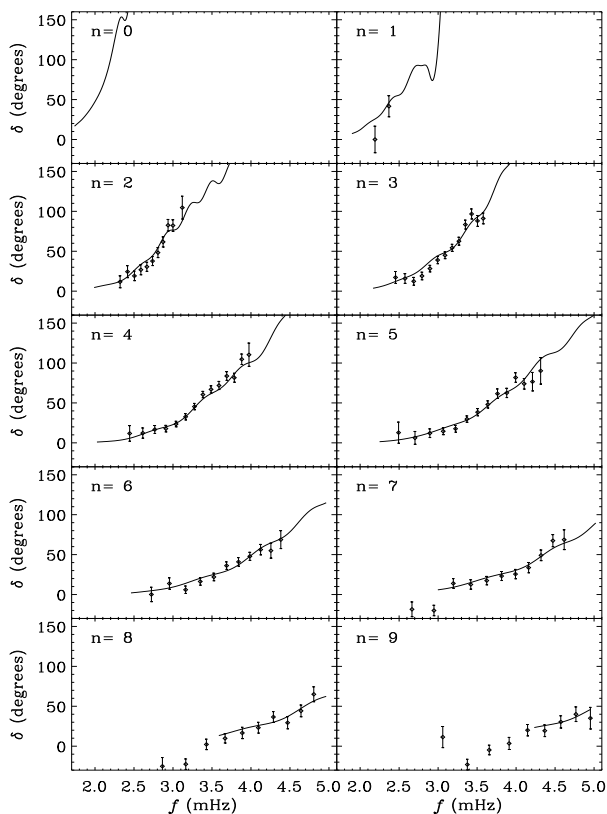


Figure 11. Phase shift δ as a function of frequency for MODEL A (Table 2) for axisymmetric modes ($m = 0$) with radial orders $n = 0, \dots, 9$ (full curves). The diamonds (and associated error bars) are the observed m -averaged phase shifts for NOAA5254 (Braun 1995). Only observational data points which satisfy our selection criteria $\sigma_\delta < 18^\circ$ are displayed.

haps the model is sensing a stronger field in subsurface layers, but we will show that the best fits to the other data sets tend to favour lower (more realistic) field strengths in general.

Figs. 11 and 12 show the phase shift δ and the absorption coefficient α as a function of frequency for MODEL A (for the axisymmetric mode $m = 0$, full curves) along with the m -averaged observations (diamonds). Fig. 11 confirms the finding of Cally et al. (2003) that the phase shifts predicted by these models are in excellent agreement with the observations ($\chi_\delta^2 \approx 1$ for MODEL A and MODEL B further support this conclusion, see Table 2). The phase shifts in Fig. 11 fit the data better than the cases presented in Cally et al. However, this is no real surprise: firstly, we have a genetic algorithm searching for the best fit on our behalf, and secondly, our model is more realistic than the complete polytrope employed by Cally et al.

The predicted absorption levels for MODEL A and MODEL B are generally ample to explain the observations for low order modes (especially at higher frequencies). For the higher order modes, the absorption produced by vertical field models is insufficient to account for the observations; however, the highly inclined field in the outer shell of MODEL A and MODEL B generates enough absorption to almost match the observed levels (at lower frequencies highly inclined fields can produce some enhancement in $\text{Im}(k)$ in

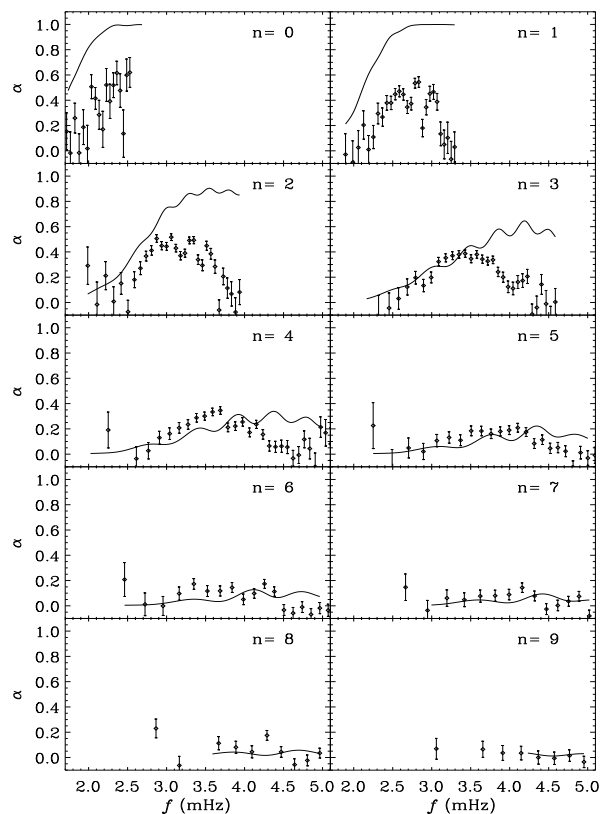


Figure 12. Same as Fig. 11 except the absorption coefficient α is plotted, and only observational data points which satisfy our selection criteria $\sigma_\alpha < 0.2$ are shown.

comparison to vertical field, see the lower right-hand panel of Fig. 7 and the upper right-hand panel of Fig. 9). Better fits for α will be found in Section 5.1.2.

As pointed out by Cally et al., the small oscillations in δ and α at higher frequencies (especially in $n = 2$ and 3) are caused by leaky resonances in the spot (partial reflections at the interfaces $r = R_s$) and would most likely be smeared out in reality. Because MODEL A and MODEL B are so alike (see Table 2) it is not surprising that the results for MODEL B (which are not displayed) are very similar to those shown in Figs. 11 and 12.

The fact that the phase shifts agree so well with observations is significant. The reduced mean travel times for waves passing through sunspots (and the closely related phase shifts) are widely believed to be indicative of a wave speed enhancement below active regions (e.g., Fan et al. 1995; Duvall et al. 1996; Kosovichev et al. 2000). Our simple magnetic models account for the thermal difference between a sunspot interior and exterior, and actually have a slightly diminished sound speed in the surface layers (due to the effect of the field, see Fig. 5). The impressive agreement between the observed and theoretical phase shifts is strong evidence that sound speed enhancements below active regions are probably not necessary – the travel time effects may be primarily magnetic in origin. As discussed in Section 1, comparisons of travel times deduced from either time-distance or holographic techniques with phase shifts determined from Hankel analysis are complicated by considerations of possible differences between the depth of the

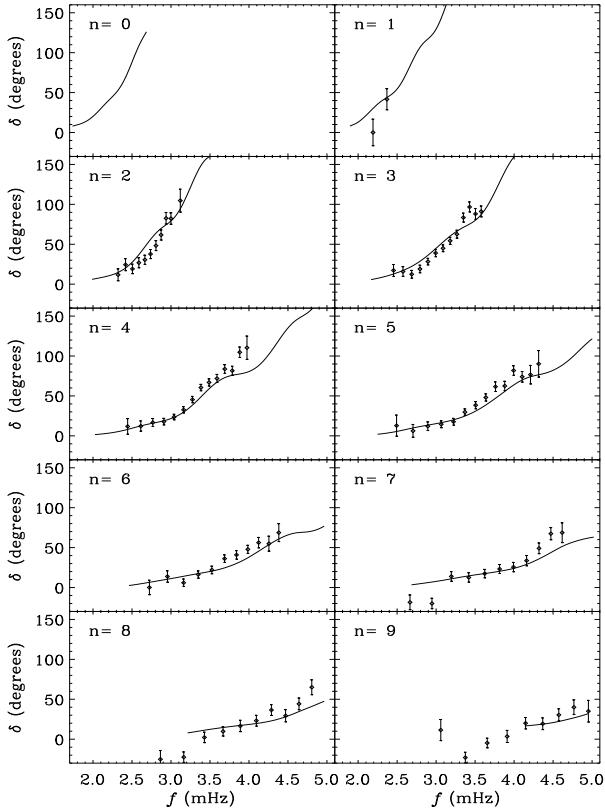


Figure 13. Same as Fig. 11 except for MODEL C (Table 3).

phase perturbations and the depth of the acoustic cavity. In general, a comparison of measurements at high degree l is particularly useful. For the highest degrees observed in Figs. 2 and 11, the observed phase shifts (with values of approximately 100°) correspond to centre-annulus travel times of approximately 50 seconds at a frequency of 3 mHz. This is comparable with both time-distance (e.g., Duvall et al. 1996; Braun 1997) and holographic (e.g., Braun & Lindsey 2000) measurements of sunspots.

5.1.2 Modelling the m -averaged phase shift and absorption data

As stated above, MODEL A and MODEL B produce absorption levels significantly in excess of the observed amount for modes with low radial orders. The α fit can be improved by requiring PIKAIA to simultaneously fit both sets of data (i.e., minimize χ_t^2 , note: there are roughly twice as many absorption points as phase shift points in this case). The parameters describing the two best models in this case are outlined in Table 3 and the graphical comparisons for MODEL C are shown in Figs. 13 and 14 (again, similar results are obtained for MODEL D but not shown).

As one would expect, the improved fit to the absorption data (Fig. 14) comes at a slight expense to the phase shift fits (Fig. 13); accordingly, the χ_δ^2 values for MODEL C and MODEL D (see Table 3) are more than double the values for MODEL A and MODEL B (Table 2), whereas the values for χ_α^2 and χ_t^2 are significantly smaller. To better fit the absorption the genetic algorithm has made four adjustments: (1)

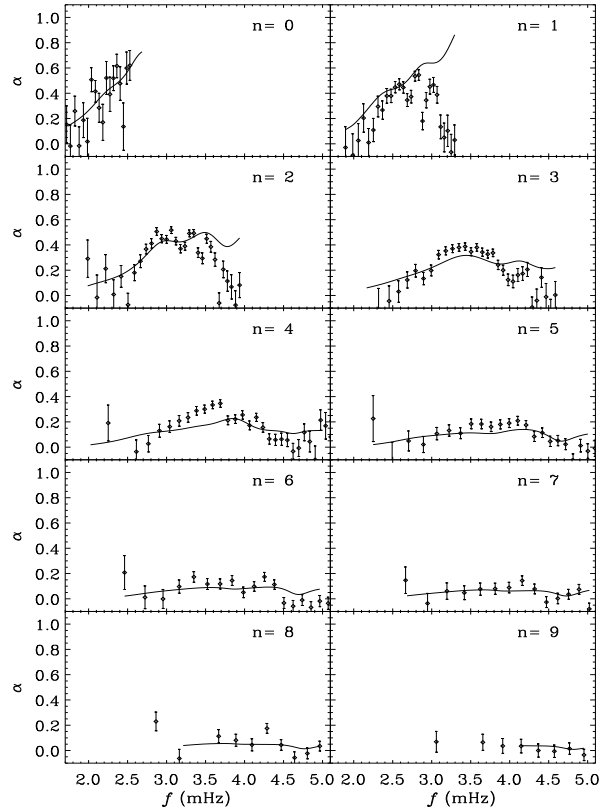


Figure 14. Same as Fig. 12 except for MODEL C (Table 3).

Table 3. The two models that produce best fits for the m -averaged phase shift and absorption data (i.e., minimal χ_t^2).

MODEL C ($\chi_\alpha^2 = 5.10$, $\chi_\delta^2 = 2.95$, $\chi_t^2 = 4.26$)

Shell	1	2	3	4	5
B_s (kG)	3	3	3	2	2
θ_s (degrees)	0	45	55	55	60
R_s (Mm)	1.00	4.10	5.78	9.23	12.53

MODEL D ($\chi_\alpha^2 = 5.35$, $\chi_\delta^2 = 2.50$, $\chi_t^2 = 4.31$)

Shell	1	2	3	4	5
B_s (kG)	3	3	3	2	1
θ_s (degrees)	0	45	60	60	60
R_s (Mm)	1.00	4.09	6.12	12.11	14.00

avoided models containing fields with $\theta \approx 30^\circ$ (where mode conversion, and hence absorption, is greatest, Fig. 9 right-hand panels); (2) favoured models with smaller total radius (because absorption scales with size, both MODEL C and MODEL D have total radii substantially smaller than the observed size of the sunspot in NOAA5254); (3) favoured models with weaker field (in comparison to MODEL A and B, because absorption also scales with B at lower and intermediate frequencies, see Fig. 8 right-hand panel); and (4) minimized the size (and hence influence) of the vertical field

Table 4. The two models that produce best fits for the m -dependent phase shift data (i.e., minimal χ_δ^2).

 MODEL E ($\chi_\alpha^2 = 4.42$, $\chi_\delta^2 = 20.25$, $\chi_t^2 = 12.34$)

Shell	1	2	3	4	5
B_s (kG)	5	3	3	2.5	2.5
θ_s (degrees)	0	20	20	20	25
R_s (Mm)	1.32	7.00	11.70	17.47	23.31

 MODEL F ($\chi_\alpha^2 = 4.49$, $\chi_\delta^2 = 20.26$, $\chi_t^2 = 12.38$)

Shell	1	2	3	4	5
B_s (kG)	3	3	3	3	3
θ_s (degrees)	0	20	20	20	25
R_s (Mm)	4.26	9.72	13.36	18.43	23.37

central core (both models have converged to the minimum allowed width of 1 Mm).

Despite being somewhat unrealistic, these models confirm what we now know about the mode conversion process: absorption produced by vertical field is too weak to account for the level observed for the high order p -modes, and the efficiency of mode conversion in non-vertical field (particularly with $\theta \approx 30^\circ$) is ample to explain the α observations. The compromise lies somewhere between the two extremes – fields with $\theta = 45^\circ$ (MODEL C and MODEL D, second shell) produce less absorption than those with $\theta \approx 30^\circ$ but still enough to account for levels experienced by higher order p -modes (see Fig. 9, right-hand panels).

For the vertical field polytrope there is a sequence of troughs in $\text{Im}(k)$ associated with the exact decoupling of the fast and slow MAG waves (and therefore a minimum in absorption, Cally et al. 1994). The troughs are present in non-vertical fields but the decoupling is not complete (Crouch & Cally 2003, 2005). By varying the equipartition depth (i.e., the field strength), Cally et al. were able to adjust the location of these troughs to roughly match the dips in α at higher frequencies. This is not feasible for the modified GONG models, because the decoupling troughs are not as common for the range of frequencies and field strengths we have examined. However, in comparison to Fig. 12, the absorption curves do a more reasonable job of reproducing the high frequency dips (especially for $n = 4 - 7$ in Fig. 14), though the peaks tend to be below the observations. The tendency of the model to favour highly inclined field (with $\theta \approx 60^\circ$ as in the outer shells of MODEL C and MODEL D) is probably due of the presence of large troughs in $\text{Im}(k)$ at roughly the same frequencies as the dips in α (see the lower right-hand panel of Fig. 7).

5.1.3 Modelling the m -dependent phase shift data

The radial structure of the regions that induce the phase shifts and absorption is best probed using a range of azimuthal orders m (Braun (1995) observed $|m| \leq 20$). For example, as the value of the impact parameter, m/k_0 , approaches the radius of the phase shifting region we expect δ

Table 5. The two models that produce best fits for the m -dependent phase shift and absorption data (i.e., minimal χ_t^2).

 MODEL G ($\chi_\alpha^2 = 2.18$, $\chi_\delta^2 = 21.05$, $\chi_t^2 = 11.62$)

Shell	1	2	3	4	5
B_s (kG)	3	3	2.5	2	2
θ_s (degrees)	0	10	10	10	20
R_s (Mm)	5.64	11.46	16.89	21.63	27.62

 MODEL H ($\chi_\alpha^2 = 1.92$, $\chi_\delta^2 = 21.32$, $\chi_t^2 = 11.63$)

Shell	1	2	3	4	5
B_s (kG)	3	3	2	2	2
θ_s (degrees)	0	5	5	10	20
R_s (Mm)	5.93	11.80	17.70	23.70	28.97

to drop off to zero (likewise for α). To this end, we now turn our attention to modelling the m -dependent data.

The two best fits for the phase shifts in this case are presented in Table 4 (no plots of these are shown). It is interesting to note that the internal parameters for MODEL E and F are quite different to those of MODEL A and B (best fits for the m -averaged phase shifts, Table 2), yet the outer radii are similar. Again, the size of the model is consistent with what has been inferred previously for the phase shifting region (Fan et al. 1995). Evidently, enough information about the total radius of the phase shifting region is retained in the frequency (and l) dependence of δ after the m -averaging is performed, despite there being reasonable variation in δ with m (indeed, the range of azimuthal orders for the averaging of δ was limited to avoid the substantial drop-off at larger m , depending on l , Braun 1995).

For MODEL E the field strength is quite high in the inner-most shell but decreases with radius, whereas in MODEL F the field strength is constant (the values are more realistic than in MODEL A and MODEL B). MODEL E and MODEL F contain only moderately inclined fields ($\theta \leq 25^\circ$). The reason for this is clear. In general, the observed phase shifts peak at $m = 0$ and drop off as $|m|$ increases. Broadly speaking, this indicates that the contribution to the phase shifts is strongest in the umbral core and weaker in the outer penumbral regions (though this point is not entirely consistent with the recent findings by holography Lindsey & Braun 2005a,b; Schunker et al. 2005, the reason for the discrepancy is unclear). In our models, highly inclined fields induce relatively strong phase shifts (Fig. 9, left-hand panels, $\theta \gtrsim 30^\circ$). Consequently, PIKAIA has avoided placing highly inclined fields in the outer shells. It is not completely obvious how to rectify this scenario. Allowing for field strengths weaker than 0.5 kG or increasing the number of shells may help, but it may be that uniform field is an inadequate assumption in the penumbra.

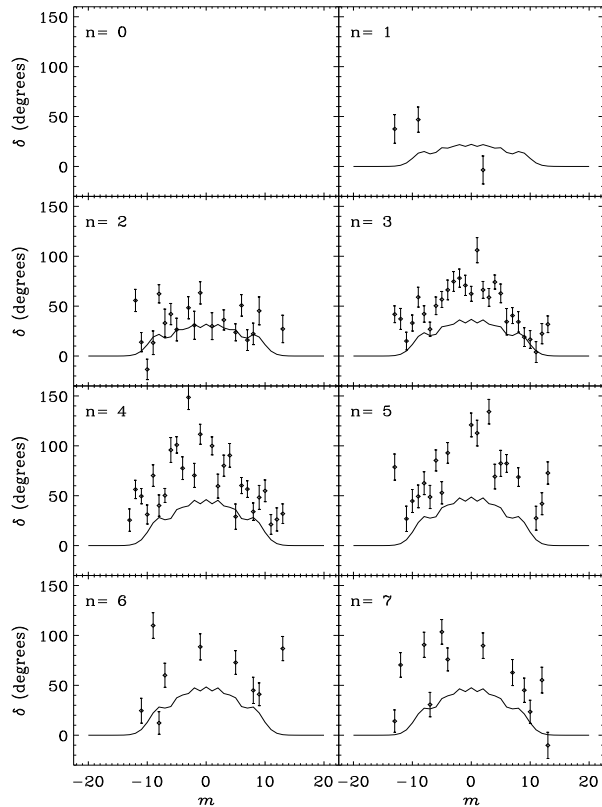


Figure 15. Phase shift δ versus azimuthal order m for modes with radial orders $n = 0, \dots, 7$ for MODEL H (*full curve*). In all of these plots the spherical harmonic degree is fixed at $l = 288$ (the frequencies for $n = 8$ and 9 are above the acoustic cutoff in this case). The *diamonds* (and associated error bars) are the phase shifts observed by Braun (1995) and satisfy $\sigma_\delta < 18^\circ$.

5.1.4 Modelling the m -dependent absorption and phase shift data

In contrast to the models for the m -averaged absorption and phase shift data (MODEL C and MODEL D, Table 3), the models for the m -dependent version of the two data types tend to be somewhat larger than the size of the actual sunspot (see MODEL G and MODEL H, Table 5). They are also larger than the models that best fit the m -dependent phase shift data alone (MODEL E and MODEL F, Table 4). To some extent, this was to be expected. Because α does not drop off substantially as m increases (in the way that δ does, see Figs. 15 – 18), we know that the absorption region is larger than both the inner radius of the Hankel annulus and the phase shifting region. This conclusion is supported by the presence of magnetic plage in the annulus (for which Hankel analysis detects some small levels of absorption but no phase shifts (Braun et al. 1988; Braun 1995), though holography finds otherwise – the source for the disagreement is uncertain). Consequently, the rather large total radii of our models is not detrimental. It does not converge to the maximum allowed radius (30 Mm, coincident with the inner radius of the Hankel annulus) because PIKAIA is also trying to fit the phase shifts (which are induced over a smaller region), rather it settles somewhere in the middle.

Graphical comparisons between the theoretical predic-

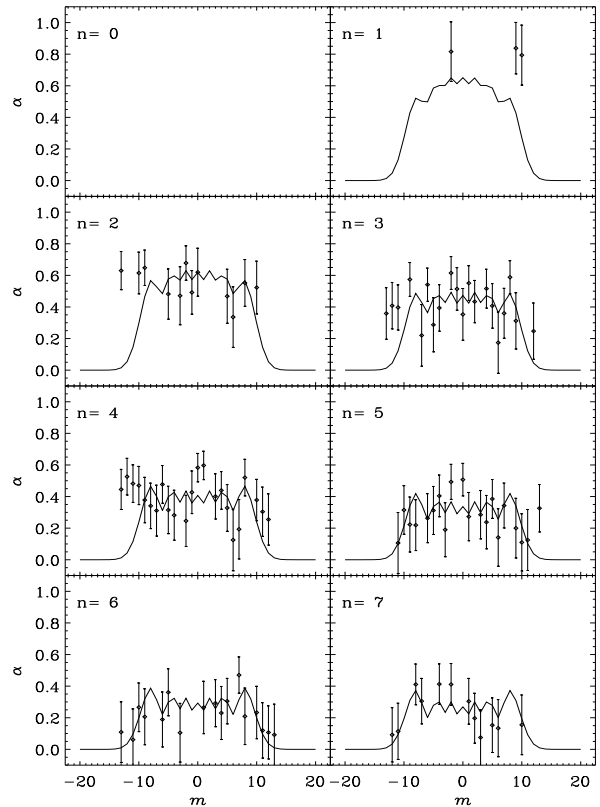


Figure 16. Same as Fig. 15 except the absorption coefficient α is plotted and only data points that satisfy $\sigma_\alpha < 0.2$ are shown.

tions of MODEL G and the observations are provided by Figs. 15 – 18, where α and δ are plotted as a function of azimuthal order m for $l = 288$ and $l = 208$ (which correspond to horizontal wavelengths of 15.16 Mm and 20.97 Mm, respectively). Because the horizontal wavelengths are roughly the scale of the spot, the results in Figs. 15 – 18 are more sensitive to the behaviour of the sunspot as a whole rather than the small-scale structure within the spot – it turns out that our models tend to perform better for these modes.

In general, MODEL G reproduces the decline in δ with m fairly well, although the magnitude of δ for modes with $n = 3 - 6$ at azimuthal orders around $m = 0$ tends to be little low. The overall decline in δ as l decreases is also well produced. However, the quality of the fits for δ (as given by χ_δ^2 , see Tables 4 and 5) are generally quite poor for the m -dependent data. On the other hand, the α fits in these cases appear to be much better (χ_α^2 is substantially lower than χ_δ^2 for both types of fits, see Table 4 and 5), though there is considerably more scatter in α than in δ .

The outer shells of MODEL G and MODEL H contain field with $\theta = 20^\circ$ which tends to absorb quite strongly (Fig. 9, right-hand panels). The presence of this can be seen as the little ‘horns’ in α at larger m in Figs. 16 and 18, which are especially noticeable for modes with higher radial orders. This outer shell presents a wide target to the incoming waves without absorbing them too much and, therefore, overcomes the preference for smaller radii in MODEL C and MODEL D (see Table 3). The presence of the vertical field (weakly absorbing) core shows up as a small (though broad) dip in α around $m \approx 0$ for the higher order modes. The phase

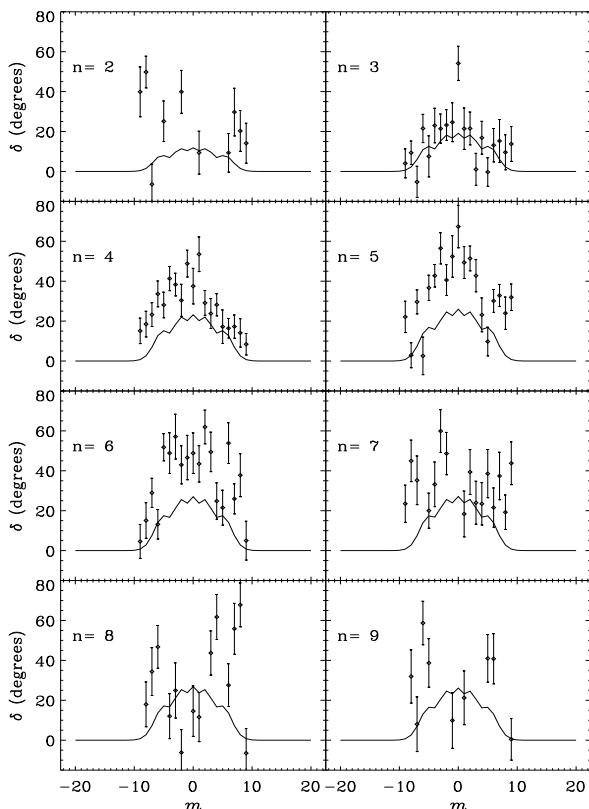


Figure 17. Same as Fig. 15 except $l = 205$ and modes with radial orders $n = 2, \dots, 9$ are plotted.

shift produced by the outer shell is much less noticeable in Figs. 15 and 17 – field inclined at $\theta = 20^\circ$ only produces a slightly different phase shift to more vertical field (see Fig. 9, left-hand panels).

6 CONCLUSIONS

We have developed a model for p -mode absorption by sunspots which, though simplistic in some respects, is much more realistic than the previous polytropic calculation of Cally et al. (2003). The model representing the convection zone includes the vertical variation of the density, pressure, adiabatic exponent, and local gravitational acceleration (along with the sound and Alfvén speeds), and properly accounts for the difference in thermal structure between a sunspot interior and exterior. Using this model, we confirmed our earlier findings (based on a complete adiabatic polytrope, Crouch & Cally 2003, 2005) that modes with radial orders $n \geq 1$ suffer significantly enhanced absorption (due to conversion to slow MAG waves and Alfvén waves) when the field is inclined at approximately 30° in comparison to vertical field (depending on the frequency and the radial order); and that the f -mode ($n = 0$) is most efficiently damped by vertical (and slightly inclined) field. Employing that realistic representation for the convection zone in conjunction with a simple model for the interaction between the f - and p -modes and the oscillations in magnetic regions (i.e., sunspots), we have confirmed that mode conversion can explain the levels of absorption observed in sunspots.

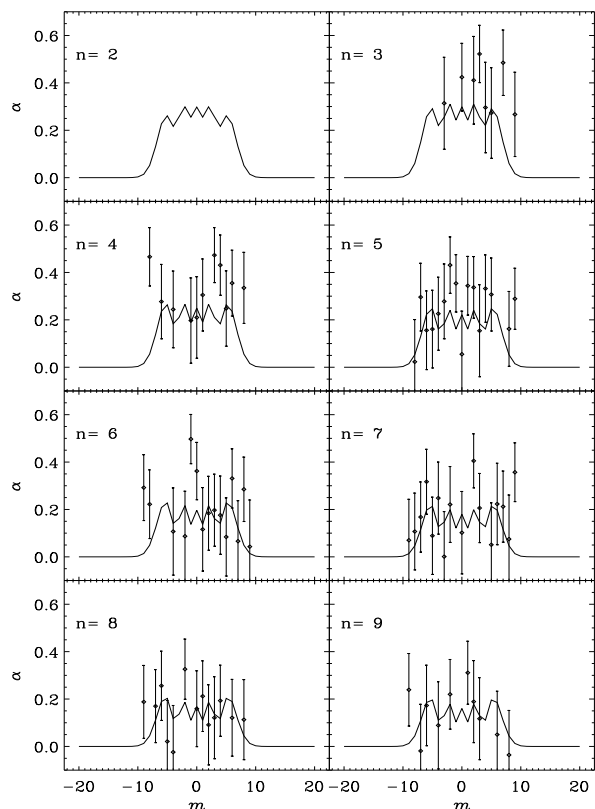


Figure 18. Same as Fig. 16 except $l = 205$ and modes with radial orders $n = 2, \dots, 9$ are plotted.

We have approached the task of testing our model as an optimisation problem, where a genetic algorithm, PIKAIA (Charbonneau 1995), searches for the set of parameters which give the best fit between the model predictions and the observations. A broad range of parameter space was tested: field inclinations up to 60° (in 5° increments), spot radii up to the size of the inner radius of the Hankel annulus (30 Mm), and field strengths $B = 0.5, 1.0, \dots, 7.5$ kG. The largest allowed field strengths are roughly twice what would be expected in a typical sunspot (such as NOAA5254), yet the fittest solutions tend to favour field strengths in the range 1 – 3 kG. In part, this confirms the validity of the model.

When the genetic algorithm is required to find the optimal fit to the m -averaged phase shifts the resultant agreement between theory and observations is remarkable (though the field strengths are a little high in those cases). The corresponding absorption levels produced by those models are generally in excess of the observations (especially at higher frequencies where the observed α drops significantly). Better fits to the absorption data can be achieved, but come at a slight expense to the phase shift fits.

Our results are also consistent with the conclusions of Lindsey & Braun (2005a,b); Schunker et al. (2005) in that a more realistic proxy for the showerglass effect is likely to require the inclusion of magnetic field inclination. In addition, we have demonstrated that highly inclined fields (with $\theta \gtrsim 30^\circ$, characteristic of sunspot penumbrae) generally induce strong phase shifts.

There are several possible reasons why we would ex-

pect our model to produce absorption in excess of the level observed by Hankel analysis at higher frequencies. Firstly, acoustic glories in the quiet Sun surrounding sunspots are strong emitters of acoustic energy (Donea et al. 2000) and may mask the real absorption produced within the sunspot (Lindsey & Braun 1999). Secondly, our model does not account for processes like the suppression of acoustic emission inside spots or convective dissipation. And thirdly, by assumption the regions responsible the absorption and phase shifts are of the same size in our model, but from the perspective of Hankel analysis they are not (due to the absorption produced by nearby magnetic plage, Braun et al. 1988; Braun 1995).

In fact, we suspect that our models themselves are underestimating the true level of absorption. We have only allowed the energy to propagate one way – *down* the magnetic field lines into the interior. There is, of course, a second option – *up* the magnetic field into the atmosphere. As we discussed, the upper boundary condition adopted in this investigation is only valid for frequencies below the acoustic cutoff frequency, ω_{ac} . However, in regions with uniform inclined magnetic fields the acoustic cutoff frequency is reduced by a factor of $\cos \theta$. We have completely ignored this effect. In our magnetic models with 2 kG vertical field $\omega_{ac} = 5.46$ mHz (greater than the non-magnetic value), but in regions with field inclined at 30° it is reduced to 4.73 mHz and if the field is inclined further (to 60°) it is more like 2.73 mHz. Therefore, in the Sun (or an improved sunspot model) it is likely that substantial amounts of acoustic energy will be lost into the atmosphere at the frequencies we considered in this investigation (e.g., Cally et al. 1994 found that to be the case for vertical field; and De Pontieu et al. 2004, 2005 have demonstrated that this process can occur in inclined magnetic flux tubes). The likely consequences of this effect on the phase shifts is less clear – we defer that calculation to a subsequent investigation.

To confirm our conclusions, several of our assumptions must be relaxed in future work: field non-uniformity should be correctly incorporated into more advanced sunspot models (e.g., Bogdan 1999; Cally 2000), and the matching across the interface separating the magnetic and non-magnetic regions should include the acoustic jacket and the possibility of mode mixing (e.g., Bogdan & Cally 1995; Barnes & Cally 2000).

It is a commonly held perception that the phase shifts and mean travel time reductions for waves travelling through sunspots (e.g., Duvall et al. 1996; Kosovichev et al. 2000) are indicative of an enhanced sound speed in the subphotospheric layers of sunspots (see also Fan et al. 1995). Our results show that this is not the only explanation – those effects may be primarily magnetic in origin. The sound speed in our magnetic models is actually slightly reduced in comparison to the non-magnetic quiet Sun model (see Fig. 5). Yet the resultant phase shifts produced by our simple sunspot models can agree remarkably well with the observations (depending on the specifics of the radial structure).

REFERENCES

- Abramowitz M., Stegun I. A., 1964, *Handbook of Mathematical Functions*. Dover, New York
- Barnes G., Cally P. S., 2000, *Solar Phys.*, 193, 373
- Bogdan T. J., 1999, *ApJ*, 512, 471
- Bogdan T. J., Cally P. S., 1995, *ApJ*, 453, 919
- Bogdan T. J., Cally P. S., 1997, *Proc. R. Soc. London*. A453, 943
- Bogdan T. J., Brown T. M., Lites B. W., Thomas J. H., 1993, *ApJ*, 406, 723
- Bogdan T. J., et al., 2003, *ApJ*, 599, 626
- Braun D. C., 1995, *ApJ*, 451, 859
- Braun D. C., 1997, *ApJ*, 487, 447
- Braun D. C., Lindsey C., 1999, *ApJ*, 513, L79
- Braun D. C., Lindsey C., 2000, *Solar Phys.*, 192, 307
- Braun D. C., Duvall T. L., Jr., LaBonte B. J., 1987, *ApJ*, 319, L27
- Braun D. C., Duvall T. L., Jr., LaBonte B. J., 1988, *ApJ*, 335, 1015
- Braun D. C., Duvall T. L., Jr., LaBonte B. J., Jefferies S. M., Harvey J. W., Pomerantz M. A. 1992, *ApJ*, 391, L113
- Cally P. S., 1995, *ApJ*, 451, 372
- Cally P. S., 2000, *Solar Phys.*, 192, 395
- Cally P. S., 2003, in *ESA SP-547: SOHO13 Workshop on Waves, Oscillations, and Small Scale Transient Events in the Solar Atmosphere: A Joint View from SOHO and TRACE*, p. 15
- Cally P. S., 2005a, *MNRAS*, 358, 353
- Cally P. S., 2005b, *Phil Trans Roy Soc Lond A*, in press
- Cally P. S., Bogdan T. J., 1993, *ApJ*, 402, 721
- Cally P. S., Bogdan T. J., 1997, *ApJ*, 486, L67
- Cally P. S., Bogdan T. J., Zweibel E. G., 1994, *ApJ*, 437, 505
- Cally P. S., Crouch A. D., Braun D. C., 2003, *MNRAS*, 346, 381
- Campbell W. R., Roberts B., 1989, *ApJ*, 338, 538
- Charbonneau P., 1995, *ApJS*, 101, 309
- Charbonneau P., Tomczyk S., Schou J., Thompson M. J., 1998, *ApJ*, 496, 1015
- Charbonneau P., Christensen-Dalsgaard J., Henning R., Larsen R. M., Schou J., Thompson M. J., Tomczyk S., 1999, *ApJ*, 527, 445
- Christensen-Dalsgaard J., 1980, *MNRAS*, 190, 765
- Christensen-Dalsgaard J., 1997, *Aarhus adiabatic pulsation package*, <http://www.obs.aau.dk/~jcd/adipack.n/>
- Craig I. J. D., Brown J. C., 1986, *Inverse problems in astronomy: A guide to inversion strategies for remotely sensed data*, Adam Hilger, Bristol
- Crouch A. D., 2003, *PhD thesis*, Monash Univ., <http://www.cspa.monash.edu.au/cspa-pub.html>
- Crouch A. D., Cally P. S., 2003, *Solar Phys.*, 214, 201
- Crouch A. D., Cally P. S., 2005, *Solar Phys.*, 227, 1
- De Pontieu B., Erdélyi R., James S. P., 2004, *Nat*, 430, 536
- De Pontieu B., Erdélyi R., De Moortel I., 2005, *ApJ*, 624, L61
- Donea A.-C., Lindsey C., Braun D. C., 2000, *Solar Phys.*, 192, 321
- Duvall T. L., Jr., D’Silva S., Jefferies S. M., Harvey J. W., Schou J., 1996, *Nat*, 379, 235
- Evans D. J., Roberts B., 1990, *ApJ*, 356, 704
- Evans D. J., Roberts B., 1992, *Nat*, 355, 230
- Fan Y., Braun D. C., Chou D.-Y., 1995, *ApJ*, 451, 877
- Jain R., Haber D., 2002, *A&A*, 387, 1092
- Jain R., Roberts B., 1994a, *Solar Phys.*, 152, 261

- Jain R., Roberts B., 1994b, *A&A*, 286, 243
Jain R., Roberts B., 1994c, *A&A*, 286, 254
Jain R., Roberts B., 1996, *ApJ*, 456, 399
Kosovichev A. G., Duvall T. L., Jr., 1997, in Pijpers F. P., Christensen-Dalsgaard J., Rosenthal C. S., eds, *Astrophys. Space Sci. Lib.*, 225, SCORE'96: Solar Convection and Oscillations and their Relationship, Kluwer, Dordrecht, p. 241
Kosovichev A. G., Duvall T. L., Jr., Scherrer P. H., 2000, *Solar Phys.*, 192, 159
Lamb H., 1945, *Hydrodynamics*, Dover, New York
Lindsey C., Braun D. C., 1999, *ApJ*, 510, 494
Lindsey C., Braun D. C., 2004, *ApJS*, 155, 209
Lindsey C., Braun D. C., 2005a, *ApJ*, 620, 1107
Lindsey C., Braun D. C., 2005b, *ApJ*, 620, 1118
Maltby P., Avrett E. H., Carlsson M., Kjeldseth-Moe O., Kurucz R. L., Loeser R., 1986, *ApJ*, 306, 284
Parker R. L., 1994, *Geophysical Inverse Theory*, Princeton University Press, Princeton
Pintér B., Goossens M., 1999, *A&A*, 347, 321
Rosenthal C. S., Julien K. A., 2000, *ApJ*, 532, 1230
Rosenthal C. S. et al., 2002, *ApJ*, 564, 508
Schunker H., Braun D. C., Cally P. S., Lindsey C., 2005, *ApJ*, 621, L149
Spiegel, E. A., Unno, W., 1962, *PASJ*, 14, 28
Spruit H. C., 1991, in Toomre J., Gough D. O., eds, *Lecture Notes in Physics*, Vol. 388, *Challenges to Theories of the Structure of Moderate Mass Stars*, Springer-Verlag, Berlin, p. 121
Spruit H. C., Bogdan T. J., 1992, *ApJ*, 391, L109
Tirry W. J., Goossens M., Pinter B., Cadez V., Vanlommel P., 1998, *ApJ*, 503, 422
Vanlommel P., Goossens M., 1999, *Solar Phys.*, 187, 357
Vanlommel P., Deboscher A., Andries J., Goossens M., 2002, *Solar Phys.*, 205, 1
Zhugzhda I. D., Dzhililov N. S., 1984, *A&A*, 132, 45
Zhukov V. I., 1997, *A&A*, 322, 302